Integrating Aircraft Performance in Traffic Flow Management Analysis for Advanced Air Mobility

Victoria Gonzalez*
University of California Irvine, 4200 Engineering Gateway, Irvine, CA, 92617, USA

Ian Levitt†
NASA Langley Research Center in Hampton, VA

Jacqueline Huynh‡
University of California Irvine, 4200 Engineering Gateway, Irvine, CA, 92617, USA

Integrating Advanced Air Mobility (AAM) into existing airspace will require substantial research and development regarding how diverse vehicles can operate cooperatively and safely in congested environments. Effective integration of AAM will hinge on the ability to develop robust, alternative traffic flow management techniques tailored specifically to the unique demands of AAM. This research introduces an air traffic management simulation framework for AAM operations, implemented in the open-source platform, BlueSky. The framework characterizes airspace through demand models and vertiport networks, and integrates high-fidelity vehicle performance and source noise models enabling a deeper evaluation of flow management methods and the connection between noise and aircraft operations for mixed fleets of unique AAM vehicles. Performance is assessed through metrics of efficiency, safety, energy usage, and community noise exposure. The framework is exercised for an example AAM airspace design in the Dallas/Fort Worth region, incorporating a departure scheduling algorithm and a conflict resolution method based on the speeds of aircraft in conflict. Results demonstrate that the speed-based algorithm resolves over 90% of arrival conflicts across all demands, though it increases energy use, particularly for faster aircraft. Results also show a reduction in community noise exposure with applying the speed-based method for mixed aircraft fleets.

I. Nomenclature

AAM = Advanced Air Mobility

*PhD Candidate, Department of Mechanical and Aerospace Engineering, AIAA Student Member
†Research Scientist, NASA Langley Research Center, AIAA Member
‡Assistant Professor, Department of Mechanical and Aerospace Engineering, AIAA Member. Corresponding Author, huynhlj@uci.edu.
Presented as Paper 2025-3637 Integrating Aircraft Performance in Traffic Flow Management Analysis for Advanced Air Mobility at the AIAA Aviation 2025 Forum, Las Vegas, NV, July 23, 2025

AC	=	Aircraft
ABEAT	=	ANOPP2 Blade Element Acoustic Tool
ADS-B	=	Automatic Dependent Surveillance–Broadcast
ANOPP	=	NASA Aircraft NOise Prediction Program
ASAS	=	Airborne Separation Assurance System
ATM	=	Air Traffic Management
BADA	=	Base of Aircraft Data
$C_{L,12^\circ}$	=	Lift coefficient at 12○ angle of attack
CD&R	=	Conflict Detection & Resolution
CPA	=	Closest point of approach
CR	=	Conflict resolution
D	=	Drag
dBA	=	A-weighted decibels
DFW	=	Dallas Fort Worth
eSTOL	=	electric Short Takeoff and Landing
eVTOL	=	electric Vertical Takeoff and Landing
FAA	=	Federal Aviation Administration
fpm	=	feet per minute
ft	=	feet
hrs	=	Hours
ICAO	=	International Civil Aviation Organization
kWh	=	Kilowatt-hour
kts	=	knotts
L	=	Lift
$L_{A,Max}$	=	Maximum A-weighted sound pressure level
lb	=	pound force
$L/D_{\max}$	=	Maximum lift to drag ratio
LOS	=	Loss of Separation
m	=	mass
m/s	=	meters per second
MSL	=	Mean sea level
N	=	Newtons

NAS	=	National Airspace System
NDARC	=	NASA Design and Analysis of Rotorcraft
nm	=	nautical miles
RPM	=	Rotations per Minute
R/C	=	Rate of climb
s_k	=	Target scheduled time for departure k
s'_k	=	Scheduled time for departure k
S_{ref}	=	Reference area
SUAVE	=	Stanford University Aerospace Vehicle Environment
T	=	Thrust
$t_{d,i}$	=	inter-arrival time between flight demands
$t_{d,k}$	=	inter-arrival time between flight demands for departure k
t	=	time
TFM	=	Traffic Flow Management
V	=	Velocity
V_{cruise}	=	Cruise velocity
$V_{L/D,max}$	=	Velocity at L/D max
$V_{\text{R/C,max}}$	=	Velocity at max rate of climb
V_{stall}	=	Stall Velocity
W	=	Weight
α	=	Angle of attack
Δt	=	target inter-departure interval time
Δt_{min}	=	minimum buffer time
λ_v	=	Departure rate at vertiport
ρ	=	atmospheric density
∞	=	Infinity
$()_{\text{L=W}}$	=	Where lift equals weight
$()_{\text{max}}$	=	Maximum

II. Introduction

Advanced Air Mobility (AAM) has the potential to revolutionize the aviation industry by expanding to markets that have historically been difficult to serve. Idealized as point-to-point air transportation within urban, suburban, and rural environments, the concept of AAM introduces a mode of transportation that can provide faster and more convenient commutes than the present-day, ground transportation options. As the population density of urban environments continues to rise [1], the stress on existing transportation infrastructure is also increasing, causing congestion and increased travel times [2]. Additionally, given the escalating concerns surrounding the climate crisis and the widespread sustainability initiatives throughout transportation sectors, there has been substantial investment towards the research and development of AAM solutions [3, 4].

There are currently dozens of AAM manufacturers worldwide developing diverse prototype vehicles, all competing to secure a leading position in a shared target market [5, 6]. These vehicles exhibit unique characteristics and were designed with varying performance capabilities, mission objectives, and operating principles. While substantial efforts and investments have focused on the development of such vehicles, the coordination of their collective operations and managing AAM air traffic is a complex problem that is only more recently beginning to be addressed [5, 7–10]. The current guidelines, regulations, and infrastructure overseeing airspace management are not directly applicable to this unique class of aircraft and the dynamic operations that will result from widespread AAM adoption [11–13]. However, foundational regulatory efforts have begun, including Engineering Briefing 105A [14], the Special Federal Aviation Regulation for powered lift aircraft [15], and the Notice of Proposed Rulemaking for enabling beyond visual line-of-sight operations of unmanned aircraft systems [11]. The diversity in vehicle design, and consequently, their performance capabilities, along with varying operator objectives poses a significant challenge for airspace integration [5]. Additionally, airspace integration of AAM presents a multifaceted challenge encompassing air traffic management (ATM), including the establishment of separation requirements, airspace operations, as well as standards for necessary ground-based and digital infrastructure, but must also consider public acceptance including community noise impact, safety, and social equity [5, 8–10].

As Advanced Air Mobility continues to evolve and integrate into existing airspace systems, policymakers, regulators, and industry stakeholders must navigate diverse operational requirements and unique airspace constraints [4]. The challenge addressed in this paper is to ensure safety and airspace efficiency with minimal power consumption and community noise impact. Understanding the impacts of substantial non-uniformity in vehicle design and performance on AAM Traffic Flow Management (TFM) is crucial for addressing these challenges. In previous work, a wide range of methodologies have been developed to address AAM vehicle design, trajectory modeling, community noise, and airspace integration, each with varying levels of fidelity. Early works by Brown and Harris [16] and Ramesh et al. [17] developed optimization-based AAM vehicle design studies incorporating simplified mission assumptions. More dynamic approaches for trajectory planning and vehicle performance, such as Ackerman et al.'s [18–20] application of MPPI control for noise-constrained real-time path generation, while NDARC [21] and SUAVE [22] have been extensively used for conceptual design and mission-based performance analysis [23, 24]. However, these platforms are not readily extensible for integrated AAM traffic simulation or for modeling existing AAM vehicle designs. Recent studies focused on airspace-level modeling and vertiport operations [2, 25, 26], scheduling [27], and conflict management strategies [28, 29]. Yet, these studies assume homogeneous vehicle fleets or lack vehicle-specific dynamics. Thus, to facilitate an informed decision-making process, this work presents an integrated modeling approach that incorporates individual AAM vehicle performance capabilities into TFM models by developing extensions to the open-source BlueSky air traffic simulation platform [30] to support multi-vehicle AAM fleet operations. Thus, a means for assessing performance metrics such as efficiency, power requirements, and community noise impact that are governed by the diverse capabilities of the AAM vehicles within a fleet mix is actualized.

The developed framework enables direct assessment of performance metrics—including operational efficiency, safety, energy usage, and community noise exposure, of which are governed by the heterogeneous performance envelopes of the distinct vehicles within a mixed fleet. As characterized in a recent publication by Jiang et al. [31], there are several simulation platforms that exist for modeling transportation systems, including both ground and air transportation. However, of the identified air traffic simulation platforms, BlueSky [30] was identified as the only open-source software that supports both vehicle performance and traffic management modeling. This framework therefore leverages BlueSky to simulate high-density AAM operations under realistic airspace and performance constraints, where an extension has been developed to realistically model the vehicle performance of AAM vehicles within BlueSky.

Through the methodology outlined, this works key contributions include a demonstration of how vehicle-specific performance limitations influence system-level airspace design and traffic management outcomes, while also providing a foundation for evaluating future airspace architectures including vehicle requirements and different combinations of traffic flow management methods. Additionally, custom performance models for three representative AAM configurations are developed and integrated into BlueSky via the OpenAP infrastructure [32, 33]. This includes performance unique to transitional eVTOL flight phases and parameterized vehicle limitations that reflect realistic energy and performance constraints. Simulated flight procedures are post-processed using kinematic models previously developed to incorporate energy consumption and community noise impact by integrating methodologies developed in [34–36]. To assess impacts of TFM methods applied to mixed AAM aircraft fleet, departure scheduling and speed-based conflict detection and resolution (CD&R) algorithms were designed and integrated into the BlueSky environment. These algorithms support intent-based detection and speed-based resolution maneuvers tailored to the dynamics and performance limitations of each unique AAM vehicle.

The framework is implemented within a NASA developed eVTOL route design in the Dallas Fort-Worth airspace [37] using scenarios of various demand rates, fleet mix, and traffic flow management protocols. The remainder of the paper is structured as follows. The methodology is detailed in Section III, outlining the methods for vehicle performance modeling in Section III.A, defining the AAM airspace definition in Section III.B, the traffic flow management methods in Section III.C, and outlining the models for estimating trajectory performance in Section III.D. A description of the analysis is presented in Section IV with the metrics for analyzing results detailed in Section IV.A. Finally the simulation results are presented in V and conclusions are drawn in Section VI.

III. Framework for integrating aircraft performance in ATM simulation for AAM

The structure of the framework for integrating aircraft performance in ATM for AAM is presented in Fig. 1, where the open-source air traffic simulation platform, BlueSky, is leveraged to perform real and fast time simulations. BlueSky was developed to provide the ATM research community with a fully open-source platform as a means for making research results more comparable [30]. Within BlueSky, new aircraft can be defined according to known performance characteristics using the integrated tool OpenAP [32] for both fixed wing and rotorcrafts; this process is described in Section III.A. Written in Python, BlueSky is composed of a user interface for visualization, and several traffic simulation modules for navigation, autopilot, and conflict detection and resolution with the implementation of ADS-B antenna feed and Airborne Separation Assurance System (ASAS). BlueSky also features many previously developed plug-ins as well as the ability for a user to define new plug-ins as needed.

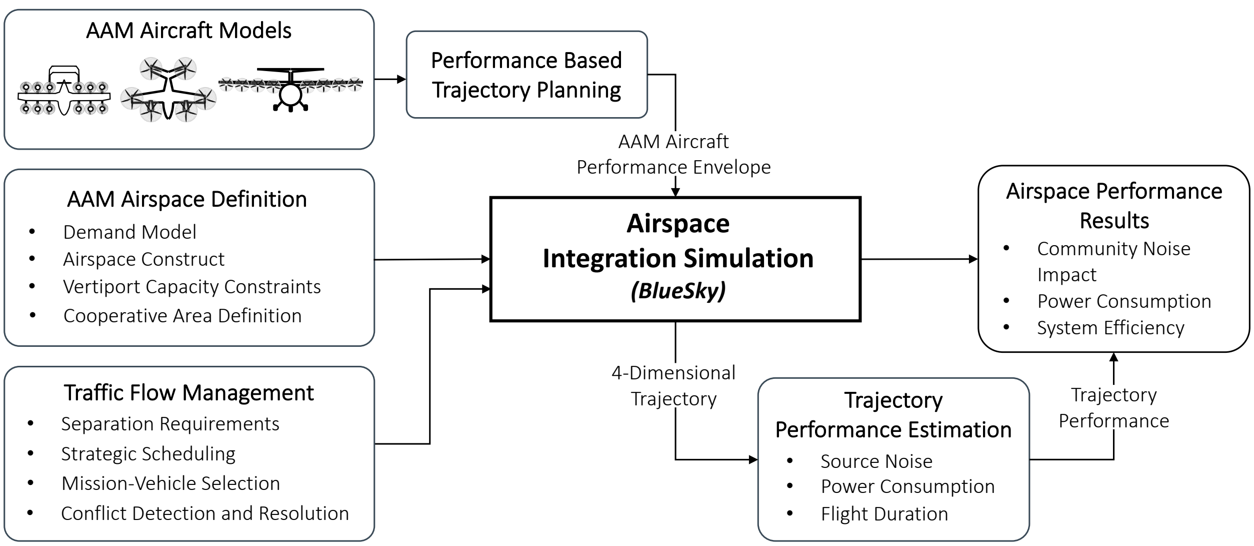

Fig. 1 AAM airspace integration simulation framework.

Within this framework, an AAM airspace is defined according to a demand model, vertiport route network, vertiport capacity constraints, and cooperative area definitions as described for the example DFW airspace in Section III.B. The definition of the airspace is input to BlueSky to simulate the airspace environment according to vehicle performance parameters defined according to the approach detailed in Section III.A, and the assigned traffic flow management methods described in Section III.C. The resulting data is collected and post-processed as a part of the Trajectory Performance Estimation to determine the collective community noise impact, power consumption, and overall system efficiency of the airspace, according to the metrics defined in Section IV.A.

A. AAM Aircraft Models and Performance-Based Trajectory Planning

Many AAM vehicle configurations are currently under development, including but not limited to Blown-Flap, electric short takeoff and landing vehicles (eSTOL), Tilt-Rotor electric vertical takeoff and landing (eVTOL) vehicles, and Lift plus Cruise electric vertical takeoff and landing vehicles (eVTOL), as depicted in Fig. 2. Each AAM vehicle has unique performance capabilities stemming from differences in configuration such as different numbers of rotors, rotor designs, placement, load capacity, aerodynamic structure, and takeoff capability.

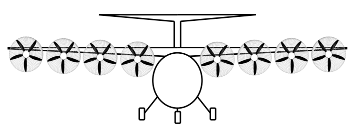

(a) Blown-Flap eSTOL

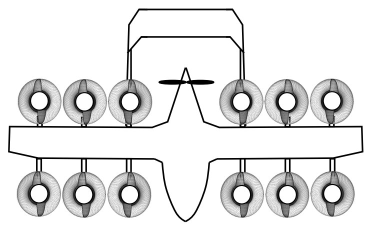

(b) Lift + Cruise eVTOL

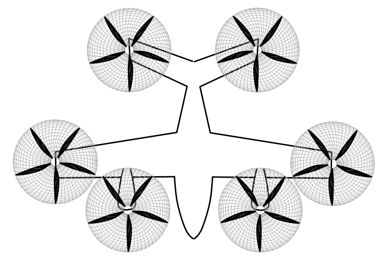

(c) Tilt-Rotor eVTOL

Fig. 2 Example AAM vehicle types. Reprinted with permission from Yeung, N., la Cruz, J. D., Pellerito, V. R., Wang, Z., Lepe, M., Huynh, J. L., and Hansman, R. J., "Flight Procedure and Community Noise Modeling of Advanced Air Mobility Flight Vehicles," AIAA Paper 2023-3361, June 2023. https://doi.org/10.2514/6.2023-3361. Copyright 2023 American Institute of Aeronautics and Astronautics/Yeung, N., la Cruz, J. D., Pellerito, V. R., Wang, Z., Lepe, M., Huynh, J. L., and Hansman, R. J.

To evaluate the impact of vehicle performance on airspace integration for AAM, it is essential to ensure that the distinct performance characteristics of each AAM vehicle configuration are accurately represented within the simulation environment. Performance characteristics for each vehicle are referenced from [38]. This allows the modeled aircraft to follow trajectories that are consistent with their true operational envelopes, enabling realistic simulation of vehicle behavior and interactions in constrained airspace. The simulation platform, BlueSky, includes several performance modeling approaches, including Eurocontrol's Base of Aircraft Data (BADA 3) and the open-source OpenAP framework [32]. While BADA is a widely used method for modeling the performance of conventional aircraft, it is unsuitable for AAM applications due to the lack of standardized data for such vehicles, which are still under development.

To address this gap, the OpenAP framework is utilized in this work. OpenAP provides a flexible interface with BlueSky to communicate performance data. In particular, it provides the WRAP model, a kinematic point-mass model that defines aircraft performance in terms of phase-specific parameters [33]. These parameters can be defined explicitly and passed directly into BlueSky, enabling simulation of AAM aircraft with non-standard or user-defined performance characteristics. Although the WRAP model was designed to extract the kinematic parameters from flight data and apply statistic model assumptions, in the context of this study the WRAP model is used as a mechanism for encoding and communicating the AAM performance envelope to BlueSky. Because flight data for AAM vehicles from industry is not yet available, necessary parameters are defined according to performance equations based on vehicle geometry and propulsion and aerodynamic characteristics defined in previous work [34, 39].

The model divides flights into discrete phases including takeoff, initial climb, climb, cruise, descent, final approach, and approach, as presented in Fig. 3 . Vertical motion is not adequately captured in the current version of BlueSky, therefore, for eVTOL vehicles, the vertical takeoff and landing phases are accounted for in scheduling and are incorporated within the models during post-processing (see Fig. 3).

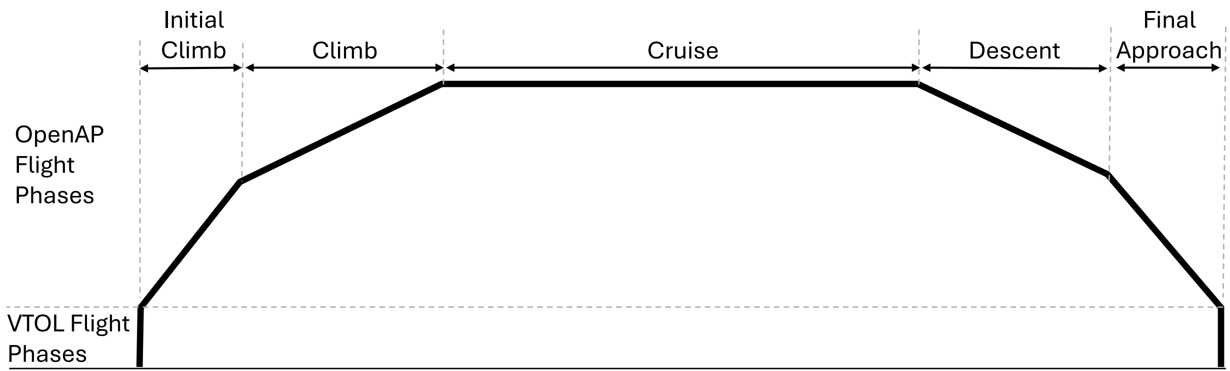

Fig. 3 AAM flight phases considered in simulation environment.

Flight phases are determined according to the vehicle's rate of climb and airspeed. As summarized in Table 1 the rate of climb distinguishes between cruise and climb, with a threshold of 20 fpm. Airspeed determines whether the aircraft is in a wing-borne flight condition. For eVTOL aircraft, this condition is governed by the minimum wing-borne flight speed, defined by eq. 1. For eSTOL aircraft, the minimum wing-borne flight speed corresponds to the flaps-up velocity, which indicates the transition to a clean aerodynamic configuration.

$$V_{\mathrm{L=W}} = \sqrt{\frac{2W}{\rho S_{\mathrm{ref}} C_{L,12^\circ}}} \tag{1}$$

The minimum wing-borne flight speed, $V_{\mathrm{L=W}}$, is defined as the speed such that the wing generates enough lift to support the weight of the vehicle, assuming $\alpha = 12^\circ$.

Table 1 Flight phase determination based on rate of climb and airspeed.

Flight Phase	Rate of Climb Range [fpm]	Airspeed
Initial climb	$[20,\infty)$	$<= V_{\mathrm{L=W}}$
Climb	$[20,\infty)$	$>= V_{\mathrm{L=W}}$
Cruise	(-20,20)	$>= V_{\mathrm{L=W}}$
Descent	$(-\infty,-20]$	$>= V_{\mathrm{L=W}}$
Final Approach	$(-\infty,-20]$	$<= V_{\mathrm{L=W}}$

For each phase of flight, the maximum and minimum velocities, climb rates, and accelerations are determined. By identifying these parameters for each phase of flight, the aircraft will operate within their performance envelopes as they are subjected to requests within the airspace, such as conflict resolution maneuvers. Table 2 depicts how each value of the kinematic WRAP model is defined for the AAM vehicles. To account for the transition phases of eVTOL aircraft, where the vehicle reconfigures between vertical flight and cruise, the parameters for the initial climb and final approach phases are defined accordingly. In the case of the eSTOL vehicle, these phases correspond to operations with deployed flaps and active blown-flap technology. For all AAM vehicle types considered, the aircraft are assumed to be in cruise configuration from the end of the initial climb phase until the final approach phase.

Table 2 Performance envelope definition according to OpenAP flight phases.

Flight Phase	Parameter	Minimum	Maximum
Initial climb	Airspeed	0	$V_{\mathrm{L=W}}$
	Climb rate	0	$\mathrm{R/C}_{\mathrm{L=W}}$
	Acceleration	0	$(T_a - D)/m$
Climb	Airspeed	$V_{\mathrm{L=W}}$	V_{cruise}
	Climb rate	$\mathrm{R/C}_{\mathrm{L=W}}$	$\mathrm{R/C}_{V_{\mathrm{cruise}}}$
	Acceleration	$-D/m$	$(T_a - D)/m$
Cruise	Airspeed	$V_{\mathrm{L=W}}$	V_{max}
	Acceleration	$-D/m$	$(T_a - D)/m$
Descent	Airspeed	V_{stall}	V_{cruise}
	Descent rate	$\mathrm{R/C}_{V_{\mathrm{stall}}}$	$\mathrm{R/C}_{V_{\mathrm{cruise}}}$
	Deceleration	$-D/m$	0
Final Approach	Airspeed	0	V_{cruise}
	Descent rate	0	$\mathrm{R/C}_{V_{\mathrm{cruise}}}$
	Deceleration	$-D/m$	0

The parameters defined in Table 2 are defined according to the vehicle performance following the propeller-driven airplane performance approach in [40]. A summary of the vehicle performance for the tilt-rotor eVTOL, the Lift plus Cruise eVTOL, and the Blown-Flaps eSTOL are presented in Fig. 4, Fig. 5, and Fig. 6, respectively. The cruise condition total drag, including both parasitic and induced drag is plotted for reference on the left. For maximum aerodynamic efficiency, the ideal cruising velocity is assigned as the velocity where L/D is maximized. This is found by evaluating the maximum of the L/D curve in the middle curve of the performance plots. Finally, the power required is plotted on the right of the performance plots, highlighting V_{max}, $V_{R/C_{\mathrm{max}}}$, V_{stall}, and the available power.

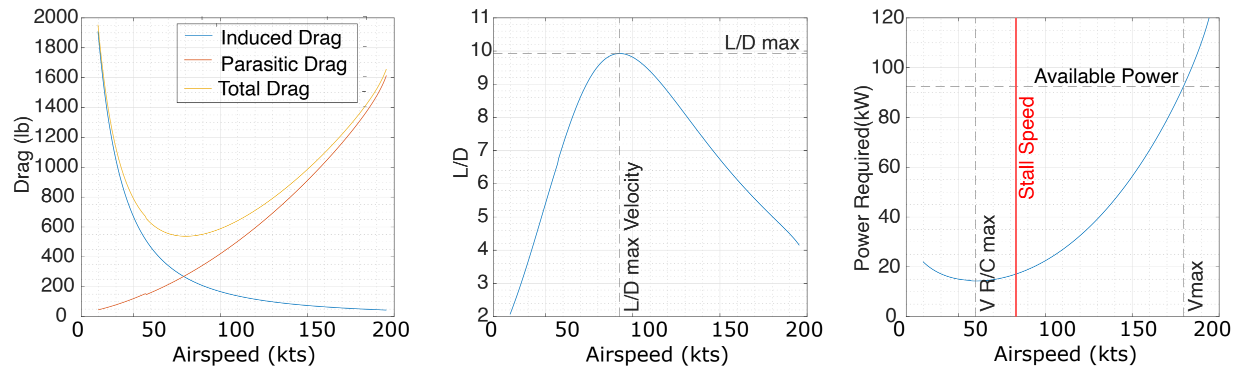

(a) Cruise drag polar **(b) Lift to Drag** **(c) Power Required**

Fig. 4 Cruise condition Tilt-Rotor eVTOL performance [38].

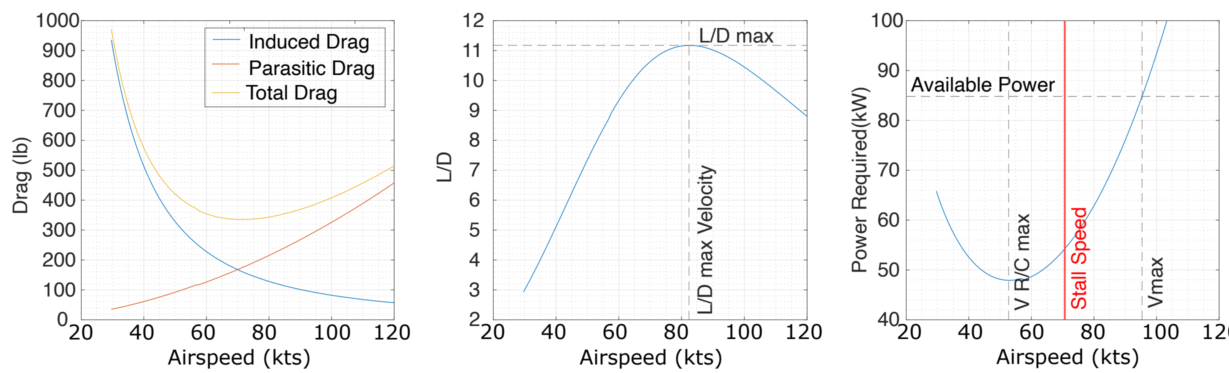

(a) Cruise drag polar **(b) Lift to Drag** **(c) Power Required**

Fig. 5 Cruise condition Lift plus Cruise performance [38].

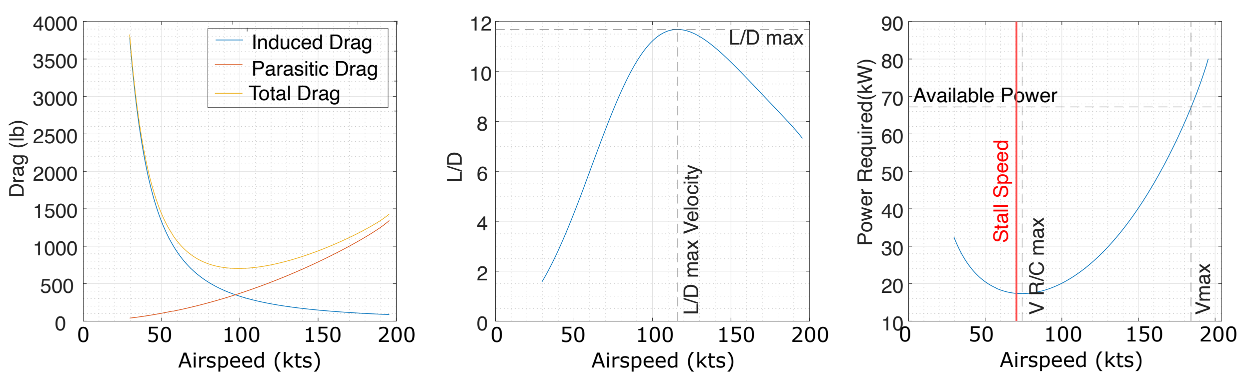

(a) Cruise drag polar **(b) Lift to Drag** **(c) Power Required**

Fig. 6 Blown-Flap eSTOL performance [38].

A summary of the performance parameters is provided in Table 3. The eVTOL vehicles both have a R/C_{max} that is obtained at an airspeed that is less than V_{stall}, thus is not achievable in cruise configuration. In this case, the ideal condition for climb is assigned to conditions for $V_{\text{L=W}}$.

Table 3 Comparison of performance parameters for tilt rotor, lift plus cruise eVTOL, and eSTOL vehicles.

Performance Parameter	Tilt Rotor eVTOL	Lift plus Cruise eVTOL	eSTOL
V_{max} (kts)	179	95	184
V_{cruise} (kts)	110	95	150
V_{stall} (kts)	83	71	58
$V_{\text{L/D,max}}$ (kts)	92	82	116
L/D_{max}	9.9	11.2	11.7
$V_{\text{R/C,max}}$ (kts)	60	53	74
R/C_{max} (fpm)	864	583	368
$V_{\text{L=W}}$ (kts)	88	75	70

The calculated parameters in Table 3 show agreement with publicly available cruise velocity specifications [41–44]. The range between V_{stall} and V_{cruise} defines the effective cruise performance envelope for each aircraft. Across these vehicles, this envelope overleaps by only a 12 kts, and reduces to 7 kts when considering $V_{\text{L=W}}$ as a safety margin above V_{stall}. This limited overlap is critical for a mixed-fleet constrained airspace.

B. AAM Airspace Definition

The AAM airspace definition consists of the airspace constructs defining the routes that AAM aircraft are permitted to fly within the airspace, specifying the cooperative areas and the regulations within them, as well as vertiport locations. The airspace construct defined for this work is detailed in Section III.B.1, and the demand model developed for the vertiports is described in Section III.B.2. This framework is modular and can be applied to other airspace constructs defined by the user.

1. Airspace Construct

This study leveraged a notional AAM airspace configuration developed for the Dallas/Fort Worth as a part of NASA's airspace research initiatives [37]. A total of 11 vertiports were selected based on engineering judgment, assigning 51 single-direction flight paths connecting them, see Fig. 7, where each vertiport origin-destination pair is assigned one set of connecting flight paths. Low-traffic routes within Class B airspace (see outline in Fig. 7) were identified as potential corridors for AAM operations such that interactions with existing air traffic would be minimized. Within these corridors, directional flight tracks were defined at 900 ft MSL altitude, spaced 1500 ft apart to accommodate a nominal track width of 1200 feet with a 300 ft buffer.

Flight tracks outside of the Class B boundary in Fig. 7 have flight level ceilings to remain below the higher altitude Class B regions. Therefore, each route is defined by latitude and longitude waypoints with maximum airspeed and altitude constraints. Although this is a preliminary design, this flight track spacing results in a 1200 ft minimum horizontal separation requirement and a 450 ft vertical separation requirement that will be used for the separation minima criteria in this study.

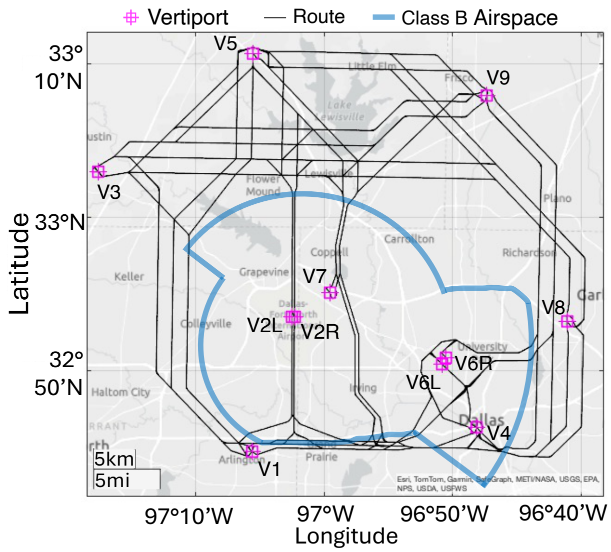

Fig. 7 Sample airspace construct for DFW, with 11 vertiports and 51 routes.

The flight tracks are defined within the BlueSky simulation environment as a series of waypoints with altitude and speed requirements imposed on the aircraft, where the speed requirements are desired, but performance limitations of the aircraft are imposed. The NASA deproach wheel design surrounds most vertiports, excluding the V2L/R and V6L/R which are located on Dallas Fort/Worth International Airport and Dallas Love Field Airport, respectively.

The AAM vehicles that are seen throughout industry have various operational constraints, applied here are range constraints and VTOL capability to meet the defined airspace constructs. The eSTOL vehicle is assumed to have a takeoff and arrival ground footprint of 150 ft [44]. To add a safety margin, veriport locations with a ground roll clearance of an arbitrary 300 ft were assumed accessible for the eSTOL vehicle. This limits the eSTOL to accessing vertiports V3, V6L/R, and V9. The range of each aircraft is identified from industry representative vehicles and are summarized in Table 4. The flight distance for each route in the network is compared to range specifications of the considered vehicles [41, 44, 45] to determine routes accessible to each aircraft.

Table 4 Available routes for each aircraft, according to range and takeoff/landing ability.

Aircraft Type	Maximum Range (nm)	Available Routes
Tilt-Rotor eVTOL	100	100%
Lift plus Cruise eVTOL	40	92%
Blown-Flap eSTOL	300	14%

2. Demand Model

A stochastic model of the demand for AAM flights is derived from a simple, but illustrative model of on-demand operations. It is assumed that passengers request a flight at the moment they are ready to go, similar to how automotive ride-sharing works today. Once a flight request is made, a departure time is determined according to the traffic flow management process in the following sections. None of the complexities and uncertainties associated with flight planning, passenger embarkment, etc., are modeled, and once a request is made by a passenger the system immediately schedules a departure as soon as possible.

While demand pressure at the vertiports could in general vary with time in this model, it is assumed without loss of generality that the number of trip requests being made by passengers per hour is constant. This allows the use of a Poisson random process for flight demand with an expected number of departures per hour at a given vertiport defined as λ_v. For each vertiport, the number of flights is sampled from a Poisson distribution:

$$N_v \sim \text{Poisson}(\lambda_v) \tag{2}$$

The time between successive passenger requests is modeled as an exponential distribution with mean $1/\lambda_v$, and each demand time is determined by the cumulative sum:

$$t_{d,i} = \sum_{j=1}^{i} \Delta t_j, \Delta t_j \sim \text{Exponential}\left(\frac{1}{\lambda_v}\right) \tag{3}$$

C. Traffic Flow Management

Applicable methods of Traffic Flow Management (TFM) for AAM are currently an on-going area of research throughout the FAA, NASA, and industry [28]. Stemming from the ICAO Global Air Traffic Management Operation Concept Document 9854 [46], a spectrum of conflict management functions range from strategic to tactical. Strategic conflict management occur earlier in the time horizon before a potential conflict, and involve tactics such as pre-departure scheduling and demand-capacity balancing of resources that occurs before or around the departure time [28]. Tactical conflict management operations occur at close time intervals to a conflict and involve inflight operation modifications deemed necessary by conflict prediction algorithms. In this framework, the TFM techniques are implemented through algorithm plug-ins to the BlueSky simulation platform. The strategic and tactical conflict management algorithms are outlined in Section III.C.1 and Section III.C.2, respectively.

1. Strategic Conflict Management through Departure Scheduling

While flight demands may follow a stochastic process, actual departure times must be coordinated to ensure operations meet required spacing for logistical and safety requirements. Given the model for how demand is generated randomly through trip requests in Section III.B.2, a first-come, first-served approach is implemented to model how departure times are determined. An artificial scheduling algorithm is designed to illustrate the framework and to demonstrate sensitivity to the captured dynamics. For this model it will be assumed that the separation applied between aircraft is able to vary, and is set proportionally to the current demand. When demand is high, the separation is reduced to accommodate more flights, and when demand is low, the separation is increased to accommodate a reduction in unplanned airborne maneuvers.

The algorithm is defined by a minimum buffer time (Δt_{min}) between successive departures, intended to reflect physical and procedural limitations at the vertiport. Additionally, a target inter-departure interval time (Δt) is defined according to the desired number of departures per hour (λ_v). This is a metered departure approach that results in higher departure separation standards for lower demand rates, reducing the reliance on tactical conflict management during flight, at the expense of increased ground delay, see Fig. 8.

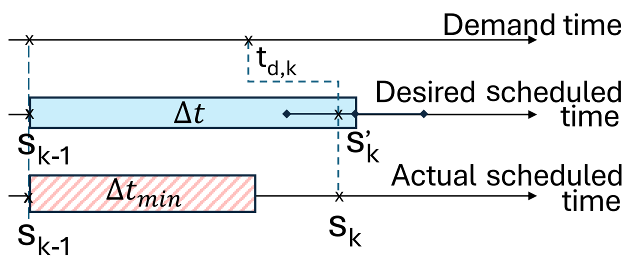

Fig. 8 Departure scheduler applied to demand a time t$_{d,k}$.

For each flight k, the the target scheduled time s'_k is modeled as a normal distribution centered at time Δt after the scheduled time for flight $k-1$ to account for error or delays:

$$s'_k \sim \mathcal{N}(s_{k-1} + \Delta t,\ \sigma^2) \tag{4}$$

The target scheduled time, s'_k, is evaluated against the requested demand time ($t_{d,k}$) and Δt_{min} to assign the actual scheduled time s_k as defined in equation 5. If the target scheduled time, s'_k is earlier than the demand time, t_d, then the aircraft is scheduled at the demand time. If s'_k is earlier than the minimum buffer time, then the departure is scheduled according to the minimum buffer time. Otherwise the aircraft is scheduled to depart at s'_k.

$$s_k = \begin{cases} t_{d,k}, & \text{if } s'_k < t_{d,k} \\ s_{k-1} + \Delta t_{\min}, & \text{if } s'_k \leq s_{k-1} + \Delta t_{\min} \\ s'_k, & \text{otherwise} \end{cases} \tag{5}$$

2. Tactical Conflict Management through conflict detection and resolution algorithms

Conflict Detection and Resolution (CD&R) protocols implemented within the simulation are performed with a lookahead time of 5 minutes. The conflict detection method applies a combined state and intent-based approach developed in [47], that is intended to mitigate false positives and false negatives of the independent approaches. The algorithm performs both a state-based conflict detection, which determines conflicts by linearly extrapolating from the current position of the aircraft along the velocity vector, within the lookahead time, and an intent-based approach which accounts for the intended route of each aircraft. A conflict is then defined as a situation where a loss of separation is predicted from both the state and intent based approaches within the lookahead time. A loss of separation (LOS) is where the minimum separation distance is breached. Since the aircraft are operating in a constrained airspace, with routes that aircraft cannot deviate from in lateral position, and with an altitude ceiling within Class B regions, the conflict resolution methods applied in this work are constrained to speed adjustments. The conflict resolution algorithm implemented is presented in Fig. 9.

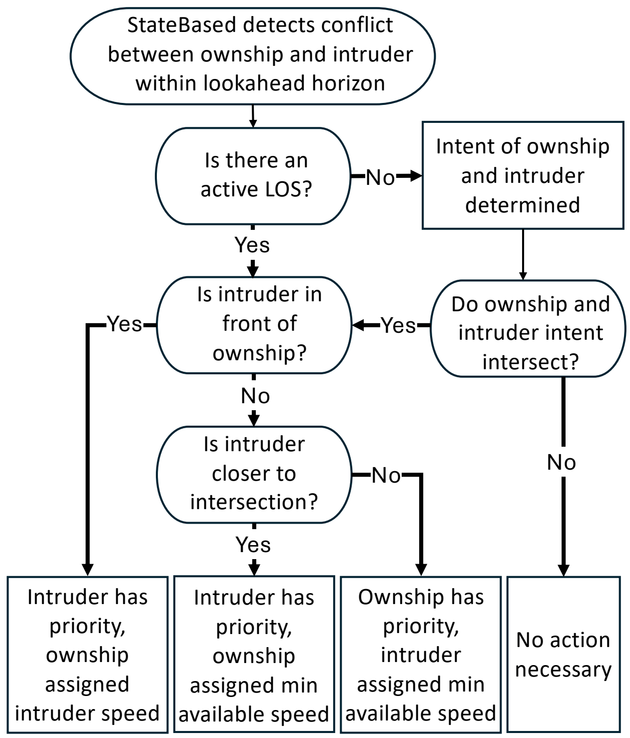

Fig. 9 Conflict detection and resolution algorithm.

When a conflict is detected by the state-based algorithm, it is evaluated to determine if there is an active LOS. If there is not, the intent of the aircraft are evaluated to determine if their paths intersect within the lookahead time. If the aircrafts' intent do not intersect, no conflict resolution action is necessary. When a conflict is confirmed by the intent-based logic, the relative position of the aircraft determines priority of the conflict. The priority is assigned to leading aircraft if they share the same flight path, or the aircraft closest to the predicted intersection point. The aircraft with lower priority is assigned the speed-based resolution. This indicates that in this scenario no passing, overtaking, of path divergence is allowed. Head-on conflicts are not accounted for because they are not possible in the defined airspace as flight paths are unidirectional. Vertical takeoff and landing maneuvers of eVTOL aircraft are not simulated or considered in the CD&R processes, but are accounted for in performance and efficiency metrics in post-processing.

D. Trajectory Performance Estimation

The trajectory performance estimation is a post-processing step following the BlueSky simulation, where the individual trajectory performance and overall airspace performance is determined according to vehicle performance metrics outlined in Section III.A. A pre-computed propulsion database developed in XROTOR [48] is referenced to determine rotor conditions which are necessary for noise and power predictions at each timestep. The time-dependent vehicle states from the BlueSky simulated flights, including speed, acceleration, climb rate, and vehicle configuration, are used to infer the rotor inflow velocity to calculate the required thrust necessary based on vehicle dynamic models from [34, 38]. The inflow velocity and thrust required are then referenced in the XROTOR database to determine the rotor state.

Power is integrated over the flight duration to compute vehicle energy consumption. A database of nominal flight operations for each aircraft–route combination within the modeled airspace is referenced as a baseline to quantify the energy and airborne delay impacts of off-nominal operations, including conflict-resolution maneuvers. Quantifying the total conflicts and losses of separation within the airspace for a given scenario detail the probability of encountering a conflict, needing to resolve a conflict, and what impact a conflict resolution maneuver has on the vehicle performance, such as a loss of energy reserves.

To estimate noise, the framework utilizes the AAM noise modeling methodology developed in [38]. This method references a database of pre-computed vehicle source noise hemispheres based on the AAM vehicles considered (Fig.2), discretized by 10 m/s inflow velocity, 100 N thrust, and 100 RPM increments, which when used for noise analysis of a flight trajectory are queried using a minimum Euclidean distance criterion over thrust and inflow velocity. The hemispheres consist of multi-rotor tonal and broadband noise, which were assumed to be the dominate sources, in the form of proportional broadband spectrum (PBS) levels. Noise was modeled using NASA's Aircraft NOise Prediction Program (ANOPP) [49] and the ANOPP2 Blade Element Acoustic Tool (ABEAT) [50]. Given rotor inflow velocity and thrust, the pre-computed XROTOR propulsion database is used to determine the associated rotor pitch and RPM for these conditions, in the case where minimum power occurs. Hemispheres are mapped to timestep t and propagated to the ground using straight-ray propagation. The observer grid was spaced by 120 meters with elevations approximated from [51].

IV. Analysis Description

The presented framework is exercised through example scenarios for the Dallas/Fort Worth airspace, demonstrating the practical application of this framework and presenting a systematic approach for evaluating operational and vehicle performance. The independent variables of this study and their variations are shown in Table 5, where a total of 12 scenario variations are included. Although other traffic flow management studies can be performed, to display the functionality of the framework this study includes simulation results for a baseline fleet with one AAM Aircraft (AC) type and a mixed fleet including the three AAM vehicle in Fig. 2. The baseline case considers the Tilt-Rotor eVTOL as the only aircraft in the system. The demand levels on the system include a nominal 10 departure requests per vertiport per hour motivated by the simulation performed in [37] and higher and lower variant at 15 and 6 requests per vertiport per hour, respectively. The demand on a vertiport is modeled as a poisson distribution with a constant mean departure rate per vertiport, outlined in Section III.B.2. A fundamental departure scheduling algorithm is developed in Section III.C.1 and scenarios are compared for applying the departure schedule and conflict resolution algorithm. Each demand level has three scenarios. One with random scheduling and no conflict resolution to provide a baseline for evaluating airspace efficiency metrics for the departure scheduling and CD&R algorithms. The addition of departure scheduling without conflict resolution and then a scenario with both departure scheduling and conflict resolution applied.

Table 5 Simulation scenarios by fleet mix, conflict resolution, scheduling method, and demand level.

Fleet Mix	Demand Level	Scheduling Method	Conflict Resolution
		Random	OFF
Baseline: one AC Type	Nominal	Departure Scheduling	OFF
		Departure Scheduling	ON
		Random	OFF
Mixed Fleet: 3 Vehicle Types	Nominal	Departure Scheduling	OFF
		Departure Scheduling	ON
		Random	OFF
Mixed Fleet: 3 Vehicle Types	Low	Departure Scheduling	OFF
		Departure Scheduling	ON
		Random	OFF
Mixed Fleet: 3 Vehicle Types	High	Departure Scheduling	OFF
		Departure Scheduling	ON

The simulation criteria outlined in Table 5 are applied using the demand model outlined in Section III.B.2 and TFM methods detailed in Section III.C. The results are analyzed in Section V according to the performance metrics outlined in Section IV.A.

A. Airspace Performance Metrics

Airspace performance of a simulated scenario is evaluated according to metrics defined to characterize demand, fleet mix, airspace safety, operational efficiency, and aircraft-level outcomes such as energy consumption and community noise exposure. Metrics that quantify simulation demand and fleet mix include:

- **Total System Demand:** The number of total flights planned for the duration of the simulation
- **Aircraft Percentage:** The percentage of demand assigned to each aircraft
- **Throughput:** the total number of flights as a function of time

For each of the demand levels in Table 5 the effects of implementing the strategic and tactical conflict management methods defined in Section III.C.1 and III.C.2 are evaluated according to:

- **Location of Conflict Detection:** Location of aircraft within constrained airspace where conflicts are detected
- **Location of LOS:** Location of aircraft within constrained airspace where loss of separation begins
- **Probability of Ground Delay:** Percentage of flights with a non-zero ground delay
- **Ground Delay Duration:** Distribution of ground delay duration over flights with non-zero delay
- **Probability of Airborne Delay**: The time an aircraft spent at non-ideal cruise state
- **Airborne Delay Duration:** Distribution of airborne delay duration over flights performing conflict resolution maneuvers
- **LOS Duration:** Total time an aircraft is in a loss of separation with another aircraft
- **Distance of CPA:** Distance between aircraft with a loss of separation at the closest point of approach

The efficiency and safety of the airspace may come at a detriment to the performance of the aircraft acting within the system. Aircraft are typically designed with the intent of operating in ideal efficiency states for majority of their operations. This becomes significant when discussing AAM vehicles as the aircraft have strict energy requirements, where operating at less efficient states can be detrimental to their range. Additionally, the open-rotor configuration can provoke excess noise pollution when operating at non-ideal rotor states. This combined with low altitude operations can result in adverse noise effects. Thus, to measure how the airspace definition and CD&R method impact the performance of individual aircraft, the following metrics are measured:

- **Energy Performance:** Additional energy spent on airborne delays caused by conflict resolution maneuvers
- **Community noise impact:** Size and location of $50N_{60}$ observer noise contours

The energy performance metric quantifies the additional energy requirements imposed by the assumed tactical conflict management algorithm defined in Section III.C.2. Community noise impact is assessed using the $50N_{60}$ metric, which is indicative of ground observer annoyance for regions close to airports, first proposed in [52]. The $50N_{60}$ measures the area where over 50 measurements of 60 dBA or more are measured within a specified time interval. Evaluating the spatial overlap between the $50N_{60}$ noise contour area and locations of conflict detection provides insight into how the implementation of the tactical conflict management algorithm influences the community noise impact for AAM operations.

V. Analysis of Simulation Results for an Example Scenario at DFW

Results for the 12 scenarios outlined in Table 5 are discussed according to the airspace efficiency, safety and vehicle performance in Sections V.A, V.B, and V.C, respectively. Figure 10 shows the throughput of the airspace in terms of simultaneous airborne flights for each demand rate, λ_v, which is modeled according to the method in Section III.B.2.

High level metrics of the different demand levels including aircraft fleet, total flights, and statistics of demand levels are summarized in Table 6. Note that the nominal demand level (λ_v = 10 in Fig. 10 and Table 6) is applied to both the baseline one AC type and mixed fleet scenarios.

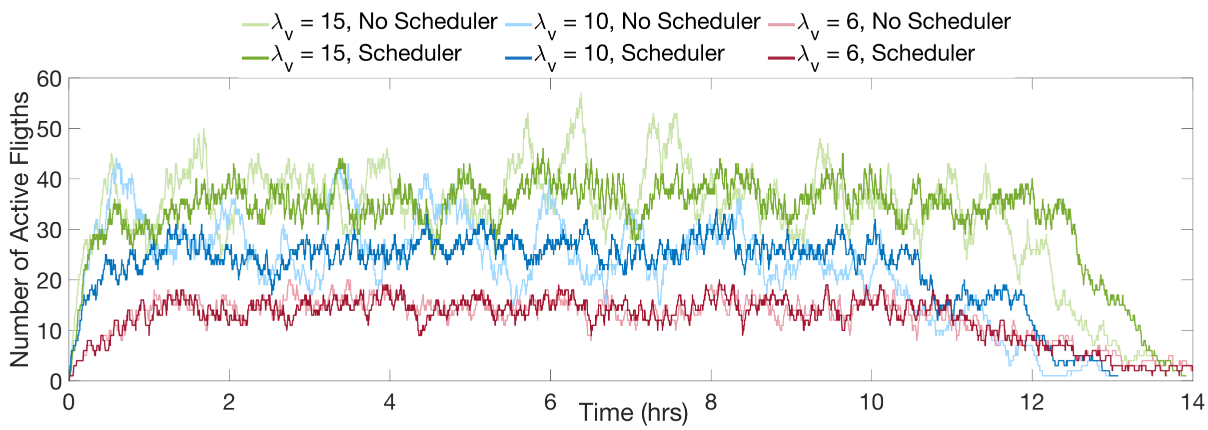

Fig. 10 Airspace throughput for demand level of 10 departures per hour per vertiport.

In scenarios with mixed fleet, vehicle assignment was modeled as a uniform, discrete random variable over aircraft types that could feasibly perform the assigned route. It is assumed that the assigned aircraft is available at the vertiport. As described in Section IV, the flight distance between vertiports for each of the 51 routes were compared against the vehicle range. If the flight distance for a route exceeded the range for the vehicle it is omitted. Additionally, the eSTOL vehicle performs takeoff and arrivals like a conventional aircraft, assuming a required a ground roll distance of 300 ft for safe operations. Therefore in this airspace, the eSTOL vehicle is limited to seven routes within the defined airspace. The lift plus cruise is assumed a range of 40 nm and is therefore restricted according to range limitations to 47 of the 51 routes.

Table 6 Distribution of aircraft configurations for each demand level.

Demand rate (λ_v)	**6**	**10**	**15**
Total Flights	594	991	1558
Percent Tilt-Rotor	50.6%	52.6%	50.3%
Percent Lift + Cruise	44.3%	42.7%	45.4%
Percent eSTOL	5.1%	4.7%	4.4%
Average Throughput- No Scheduler	13	23	33
Average Throughput- Scheduler	13	23	33
Peak Throughput - No Scheduler	20	44	57
Peak Throughput - Scheduler	20	34	46

Comparing the active flights plotted in Figure 10, the effects of applying the scheduling method outlined in Section III.C.1 is apparent. The number of active flights in the system becomes more stable, while the average throughput of the system remains the same, evident in Table. 6. All scenarios under the same demand rate imply the same demand input to provide consistency when evaluating results.

A. Airspace Efficiency

The airspace efficiency is evaluated according to the probability of experiencing ground and airborne delays, and the resulting energy impacts of airborne delays. The scenarios examine implementing an open loop departure scheduler with no feedback from the system regarding potential hazards, conflicts, or implementing schedule times of arrivals. This is a sample scheduling method and is not intended to be a complete solution to AAM scheduling. When applying the scheduling method presented in Section III.C.1, the probability distribution of a ground delay as a result of the departure scheduling imposed on the demand at each vertiport is presented in Fig. 11 for each demand rate, and a summary is compiled in Table 7.

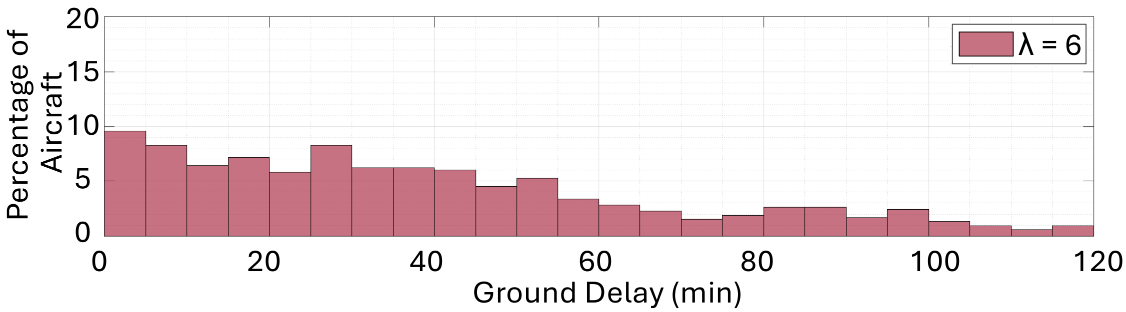

(a) Distribution of ground delay for demand level λ_v = 6

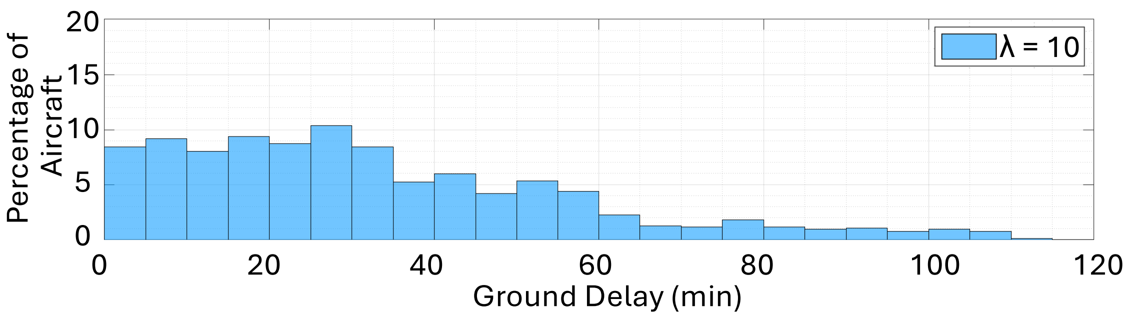

(b) Distribution of ground delay for demand level λ_v = 10

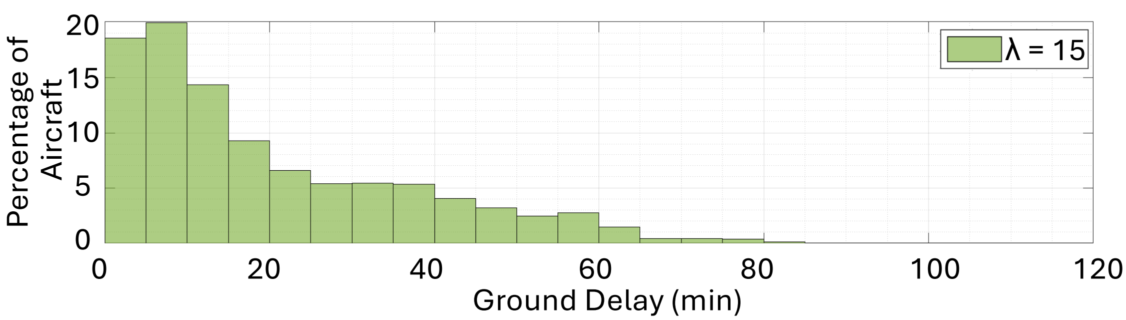

(c) Distribution of ground delay for demand level λ_v = 15

Fig. 11 Distribution of ground delay for different vertiport demand rates λ_v where the results of departure metering are evident in larger scheduled delays for lower demand rates.

The scheduler was designed to account for the desired demand of the system, imposing a departure metering effect where the nominal time between successive flights is dictated by the demand rate. The effects of this is apparent in the large delays for the low demand rate, λ_v of 6, and low delays for the high demand rate. When the required separation between successive flights is lower, i.e. for the higher demand rate (λ_v of 15), the resulting ground delay is lower even though there is a higher demand on the system. In which case there is a higher reliance on tactical conflict management to mitigate conflicts in the system.

Table 7 Ground delay resulting from departure scheduler.

Scenario	**Mixed Fleet**	**Mixed Fleet**	**Mixed Fleet**
Demand	λ_v **= 6**	λ_v **= 10**	λ_v **= 15**
Pct. of Aircraft with Ground Delay	89%	94%	90%
Avg. Ground Delay (min)	39	33	20
Peak Ground Delay (min)	120	110	83.7
Std. Dev. of Ground Delay (min)	29.4	24.1	17.3

The distribution of airborne delay resulting from a conflict resolution maneuver applied according to the conflict resolution algorithm defined in Section III.C.2 is presented in Fig. 12 for each demand scenario. The conflict resolution algorithm defined for this study is a simplified algorithm that is not intended to be complete, but is rather an example to depict how it can be studied in this methodology. Relevant statistics are summarized in Table 8. The results show that it is more likely to experience airborne delay at higher demand rates, where the average delay is higher and there is larger variability in delay. Additionally, there is an increase in delay time and variability for mixed fleet.

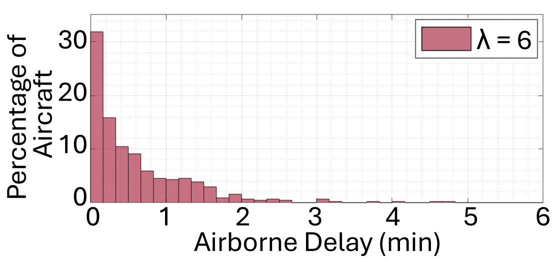

(a) demand level λ_v = 6

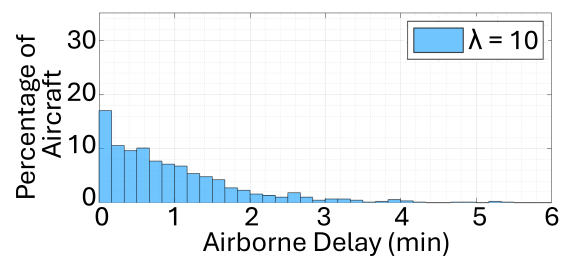

(b) demand level λ_v = 10, mixed fleet

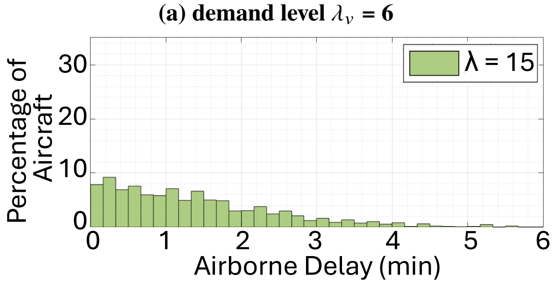

(c) demand level λ_v = 15

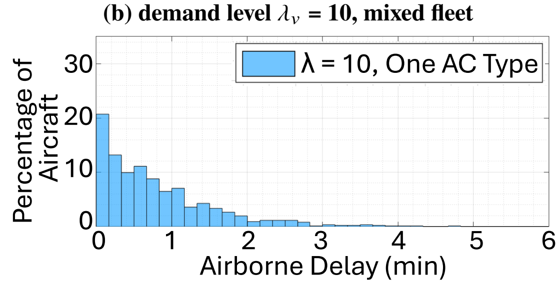

(d) demand level λ_v = 10, one AC type

Fig. 12 Distribution of airborne delay for different demand levels and fleet mix.

Table 8 Summary of airborne delay resulting from conflict resolution maneuvers.

Scenario	**Mixed Fleet**	**Mixed Fleet**	**Mixed Fleet**	**one AC type**
Demand	λ_v **= 6**	λ_v **= 10**	λ_v **= 15**	λ_v **= 10**
Pct. of AC with Airborne Delay	74%	87%	95%	87%
Avg. Airborne Delay (min)	0.62	0.96	1.40	0.79
Peak Airborne Delay (min)	4.8	6.1	8.2	4.8
Std. Dev. of Airborne Delay (min)	0.69	0.89	1.08	0.75

The distribution of energy spent on airborne delay is presented in Fig. 13, with statistics shown in Table 9. The energy spent on delay for majority of the conflicts detected require additional energy consumption of less than 5 kWh. However, this does not necessarily indicate that the conflict was resolved by the maneuver. This speed-based conflict resolution algorithm requires the aircraft assigned the resolution to reduce its airspeed either to the minimum allowable airspeed or to match the speed of a leading aircraft. In some instances, this may lead the aircraft to adopt a more energy-efficient speed for part of the trajectory. As a result, a maneuver that introduces a significant time delay may not correspond to a proportional increase in energy consumption. Moreover, scenarios with higher traffic demand tend to show greater excess energy use and variability. This is likely attributable to the increased frequency of conflicts per aircraft, which induces repeated acceleration and deceleration as new conflicts are encountered throughout the flight.

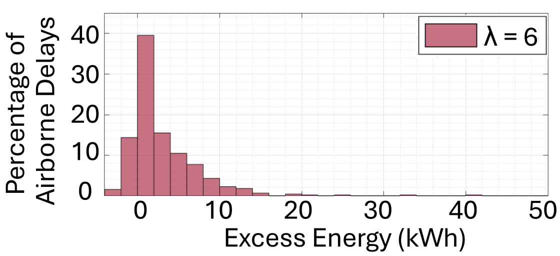

(a) demand level λ_v = 6

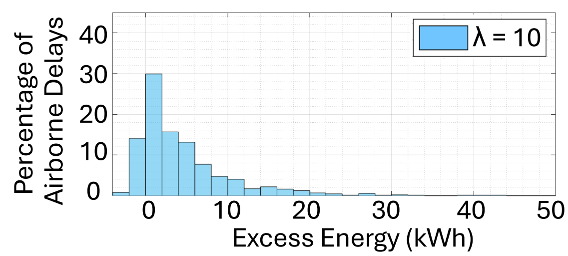

(b) demand level λ_v = 10, mixed fleet

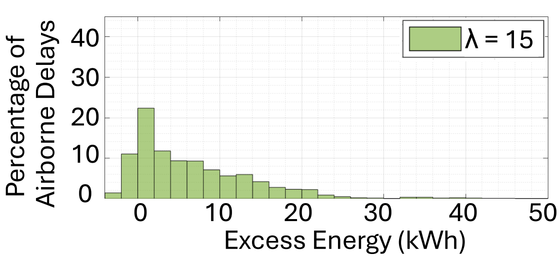

(c) demand level λ_v = 15

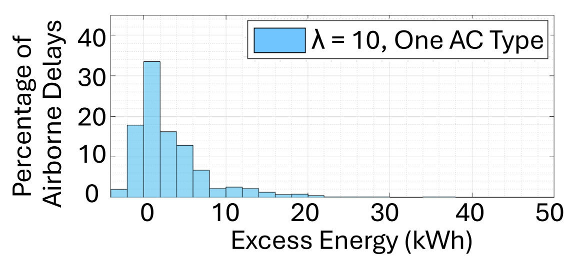

(d) demand level λ_v = 10, one AC type

Fig. 13 Distribution of energy spent on airborne delay due to conflict resolution maneuvers for different demand levels and fleet mix.

Table 9 Summary of energy spent due to airborne delay caused by conflict resolution maneuvers.

Scenario	Mixed Fleet	Mixed Fleet	Mixed Fleet	one AC type
Demand	λ_v = 6	λ_v = 10	λ_v = 15	λ_v = 10
Avg. Energy spent on delay (kWh)	3.08	4.5	6.9	3.2
Peak Energy (kWh)	40.5	31.6	50.7	37.4
Std. Dev. (kWh)	4.5	6.0	8.7	4.77

B. Airspace Safety

Airspace safety is evaluated according to the number of losses of separation (LOS) and their severity, measured by the distance at the closest point of approach (CPA), and the duration of the LOS. Conflict locations are analyzed using maps of detected conflict and LOS events for each scenario. As shown in Fig. 14 for the single aircraft type scenario, it is evident that a significant area of conflict is the inlet and exit of V2L/R at DFW airport, where two parallel routes of opposite flow are separated by only 980 ft, which is less than the 1200 ft horizontal separation standard assumed for the airspace. Although the conflict detection algorithm includes intent, a LOS is still registered for aircraft passing on these closely spaced routes. Additionally, conflict hotspots are observed at vertiports and the intersections on the south end of the airspace. These findings suggests the need for scheduled arrival times in future scheduling algorithms.

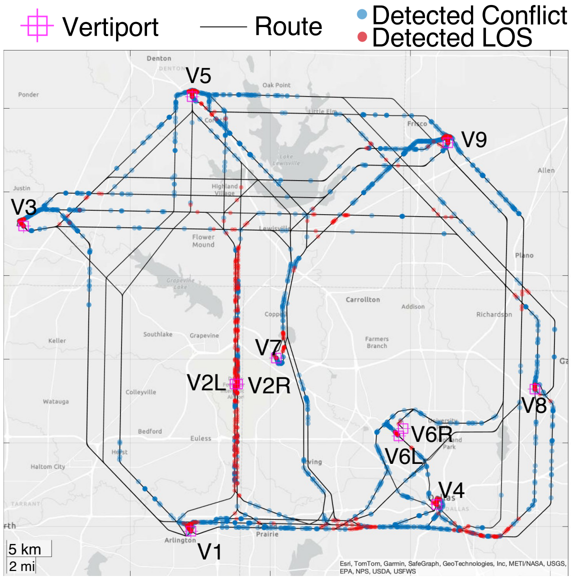

(a) Random Demand

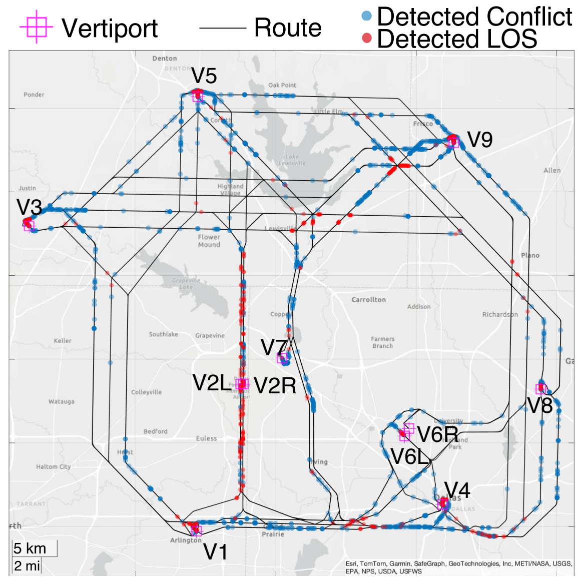

(b) Departure Scheduling

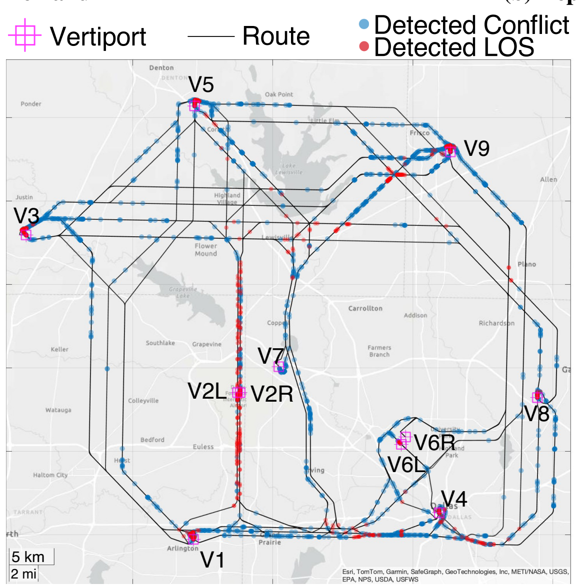

(c) Conflict Resolution Algorithm

Fig. 14 Map of conflict and LOS locations in DFW airspace for demand level λ_v = 10, one AC type.

When comparing Figure 14c to the maps without conflict resolution on (Fig. 14a and b), majority of the LOS that remain include arrivals into vertiports, and the routes into DFW. This suggests that speed-based conflict resolution is not sufficient in areas close to the vertiport, as aircraft are already decelerating, limiting the control authority over airspeed and minimizing the ability to perform CR maneuvers. Additionally, as discussed in Section V.A, the simplified conflict resolution algorithm does not effectively resolve conflicts for decelerating aircraft as the priority is assigned to aircraft closer to the CPA, which for aircraft decelerating at different rates, may change. Results are comparable for the remaining scenarios with a significant increase in density for the high demand scenario of $\lambda_v = 15$.

Conflicts and LOS events are categorized by location and vehicle flight phases for understanding the effectiveness of the CD&R algorithm. Four categories are considered: (1) shown in Fig. 15a LOS events between two aircraft on approach into the same vertiport (A-A), (2) in Fig. 15b are events between aircraft on approach and departure at the same vertiport (A-D), (3) Fig. 15c shows events between aircraft neither on approach nor departure (C-C), and (4) Fig. 15d are events within Class B airspace caused by airspace design constraints.

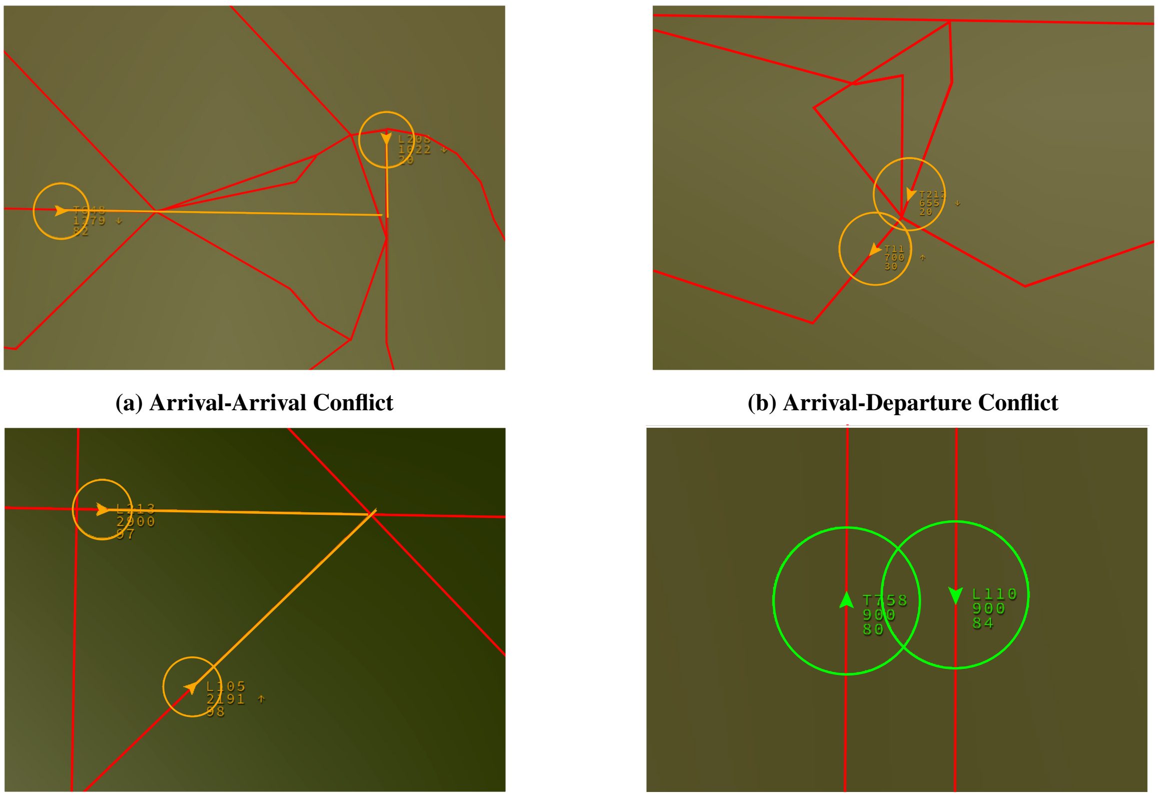

(a) **Arrival-Arrival Conflict**

(b) **Arrival-Departure Conflict**

(c) **Cruise-Cruise Conflict**

(d) **Class B Airspace Conflict**

Fig. 15 Example of categorized conflicts for (a) arrivals, (b) arrivals and departures, (c) cruise, and (d) class B airspace.

The Class B LOS events are not detected by the conflict detection algorithm, as the intent-based logic requires predicted path intersections within the lookahead time. Figure 16 presents the conflict resolution rate for each category across different demand scenarios. Note, the Class B LOS events are not detected by the CD algorithm and thus not captured in Fig. 16.

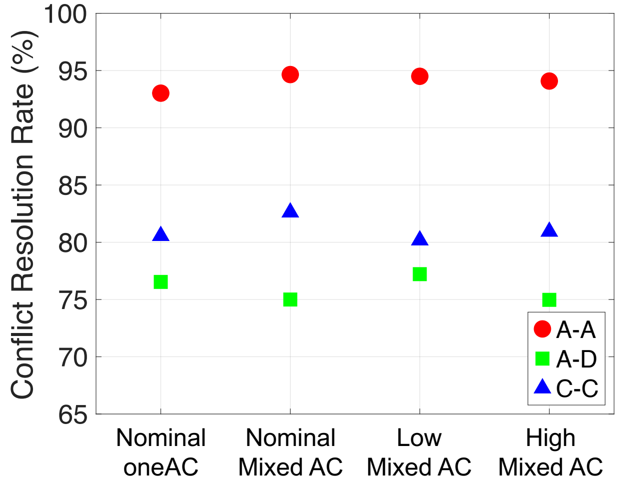

Fig. 16 Percent of detected conflicts resolved from conflict resolution algorithm for each demand scenario, categorized by conflict location and flight phases.

Across the demand scenarios, the CR algorithm resolves over 93% of the detected conflicts on arrivals, 80 - 83% of C-C conflicts, and around 75% of A-D conflicts. The severity of LOS events that are not resolved by the algorithm is characterized by the closest point of approach (CPA) distance and LOS duration. Resulting trends for the different conflict categories comparing the LOS severity for CR on and off are presented in Fig. 17 for the nominal demand rate and one aircraft type. On conflicts that are not resolved, it is desired that the CD&R algorithm improve the severity of a conflict by decreasing the duration of the LOS and increase the CPA distance. Given that the algorithm is known to not identify Class B conflicts and is provided no information about departures, the Class B and A-D conflicts are expected to not perform well.

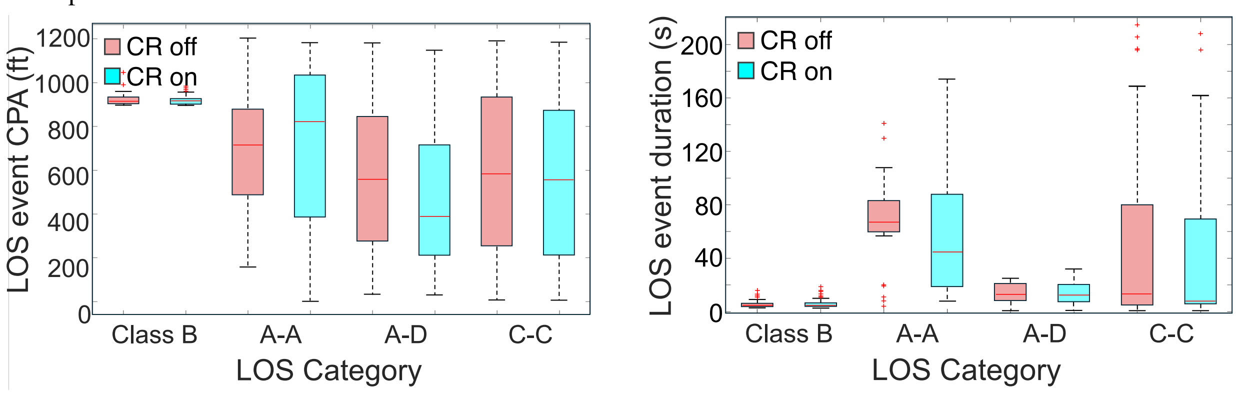

(a) LOS closest point of approach **(b) LOS duration**

Fig. 17 Severity of LOS events for nominal demand level (λ_v = 10), one AC type.

The Class B conflicts result from the airspace construct, particularly the parallel routes into DFW, where the separation distance is less than the minimum horizontal separation requirement (see Fig. 15d). Consequently, aircraft on these routes experience LOS events that the intent-based logic of the CR algorithm cannot detect, as the routes do not intersect. These events exhibit minimal variability in severity and are largely unaffected by the conflict resolution algorithm. Loss of Separation events occurring between aircraft on arrival present trends of an increased CPA distance and decreased duration as a result of the CR algorithm, however the variability increases. For LOS events between aircraft arriving and departing from the same vertiport (A-D), the CPA has a decreasing trend with minimal change in the duration. The remaining C-C conflicts present a minimal decrease in CPA distance and duration. The LOS severity results for the nominal demand, mixed fleet is presented in Fig. 18.

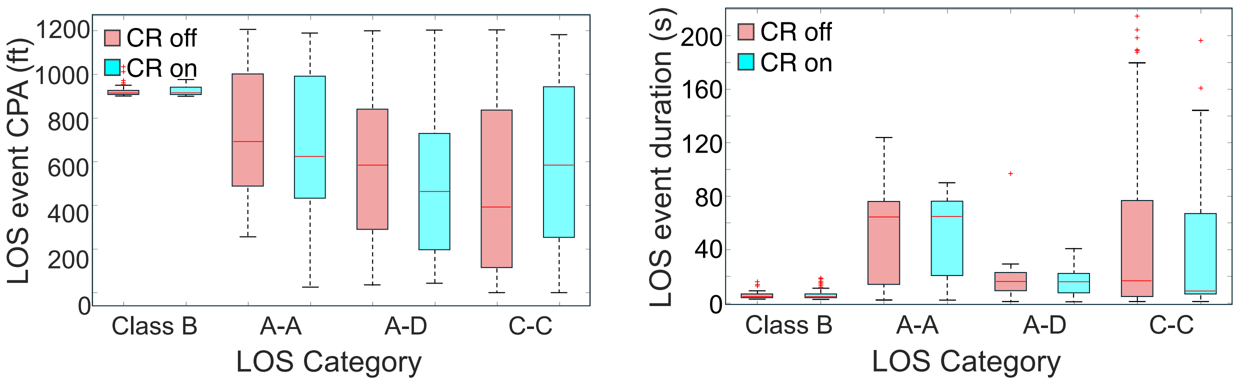

(a) LOS closest point of approach **(b) LOS duration**

Fig. 18 Severity of LOS events for nominal demand level (λ_v = 10), mixed fleet.

Similar trends for the Class B conflicts are apparent. LOS events for aircraft on arrivals present a decreasing trend in CPA distance with increased variability and minimal change in duration, but with decreased variability. The A-D LOS events present a decrease in CPA distance and a decrease in duration, but with increased variability. The C-C LOS events show increased CPA distance and decreased durations, showing the severity is trending in the safer direction. The results are presented in Fig. 19 for the low demand scenario, mixed fleet.

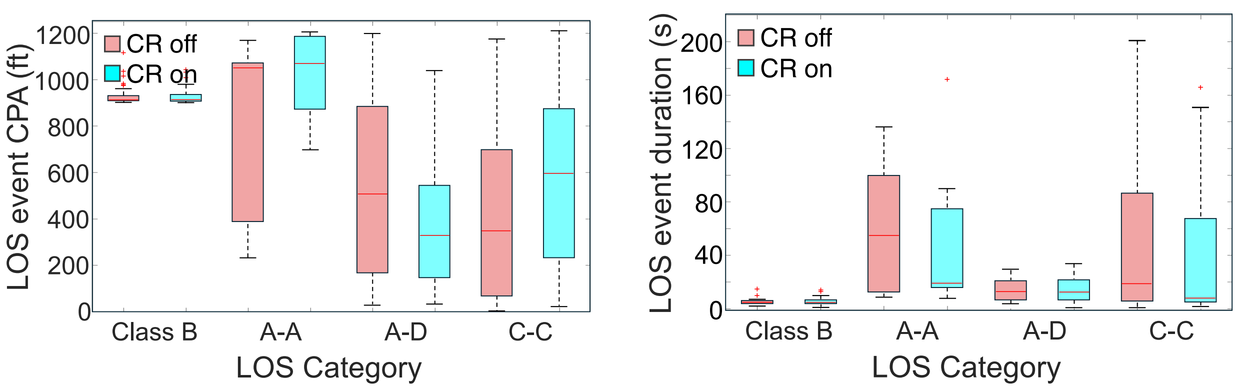

(a) LOS closest point of approach **(b) LOS duration**

Fig. 19 Severity of LOS events for low demand level (λ_v = 6), mixed fleet.

Similar trends are present for Class B conflicts. LOS events for aircraft on arrivals present a decreasing trend in CPA distance with increased variability and increased duration, with increased variability. The A-D LOS events present a decrease in CPA distance and a decrease in duration, but with increased variability. The C-C LOS events show increased CPA distance and decreased durations, showing for conflicts outside of the vertiport airspace the LOS severity is trending in the safer direction. Lastly, the results for the high demand scenario, mixed fleet is presented in Fig. 20.

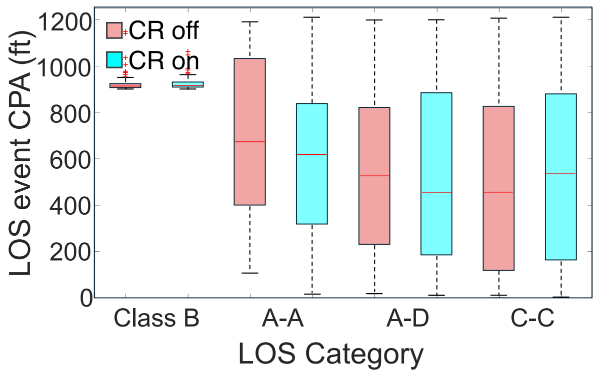

(a) **LOS closest point of approach**

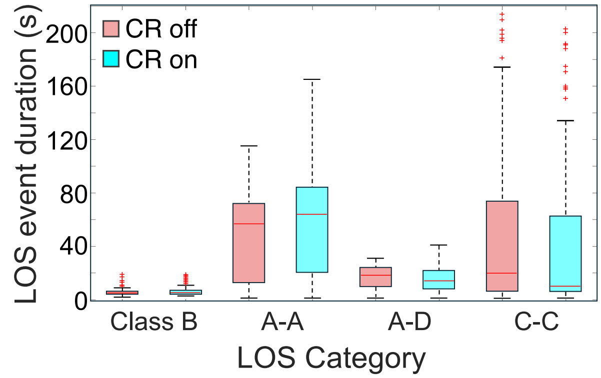

(b) **LOS duration**

Fig. 20 Severity of LOS events for high demand level (λ_v = 15), mixed fleet.

Like the previous demand scenarios, there is negligible impact of CR algorithm to the Class B conflicts. LOS events for aircraft on arrivals present a decreasing trend in CPA distance with increased variability and increased duration, with increased variability. The A-D LOS events present a decrease in CPA distance and a decrease in duration, but with increased variability. The C-C LOS events show increased CPA distance and decreased durations, suggesting that for conflicts outside of the vertiport airspace the LOS severity is trending in the safer direction.

The results indicate that the CR algorithm resolves over 93% of conflicts detected between aircraft arriving into the same vertiport. The departure metering effects from the departure scheduler in the low demand scenario effectively lowers the reliance on the CD&R algorithm and the severity of conflicts improve across both metrics considered. The remaining unresolved conflicts suggest limitations in the algorithm's effectiveness. This could be a result of a loss of control authority over speed adjustments during descent, where aircraft are already decelerating and unable to further reduce speed. Additionally, a "bouncing" effect of priority assignment shifting between the two aircraft is evident in cases where aircraft are similar distances away from the CPA, which could be mitigated with feedback on priority assignment. Furthermore, the fixed 5-minute lookahead time when arriving into a vertiport where the route design presents abrupt changes to aircraft heading can result in a high number of false-positive conflicts due to the state-based conflict detection, given that the intent-based logic confirms routes intersect as they enter the same vertiport. These observations suggest the need for design decisions around scheduled times of arrival into vertiports, and shorter lookahead times may be required on arrivals due to the increase in heading changes and reduced aircraft speeds.

C. Vehicle Energy Performance

Vehicle energy performance is measured according to energy spent on airborne delays. The summary of energy spent on airborne delay for each demand scenario presented in Figure 13 is expanded on here to determine how these results impact individual aircraft types within mixed fleet scenarios. Thus, the distribution of energy spent on airborne delay is presented for the low demand, nominal demand rate, and high demand rate for a mixed aircraft fleet in Figures

21-23. The one AC type scenario is not assessed in this section given that the fleet consists of only the tilt-rotor vehicle.

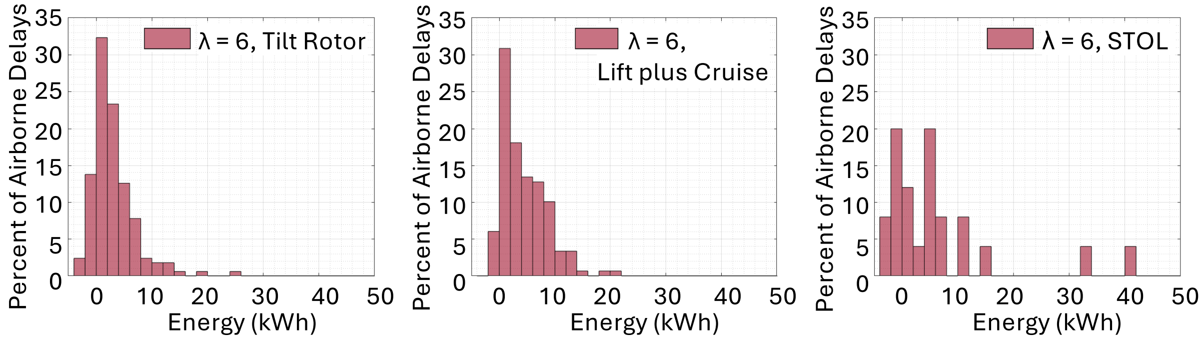

(a) Tilt Rotor eVTOL **(b) Lift plus Cruise eVTOL** **(c) Blown-Flap eSTOL**

Fig. 21 Energy spent on airborne delay per aircraft for demand scenario λ_v = 6, mixed fleet.

The results for the low demand rate (λ_v = 6) are summarized in Table 10. Both eVTOL configurations present a similar probability of encountering airborne delay, at 56%. However, the lift plus cruise configuration shows a higher average energy consumption for delays compared to the tilt-rotor. The eSTOL vehicle exhibits a significantly higher likelihood of experiencing airborne delay, with 86% of flights effected, and the energy spent on delay presents even greater variability, reflecting higher uncertainty. However, as evident in Figure 21, nearly 30% of the airborne delays for the eSTOL and 20% for the tilt-rotor resulted in a reduction in energy consumption. This behavior arises because these vehicles operate at higher cruise speed than the lift plus cruise, and for conflicts that occur on arrival, the resolution maneuvers may require earlier deceleration without subsequent acceleration, leading to a net energy savings.

Table 10 Summary of energy spent on airborne delay per aircraft for demand scenario λ_v = 6, mixed fleet.

Configuration	Tilt Rotor	Lift plus Cruise	eSTOL
Flight Count	300	264	30
Flight with Airborne Delay	167	149	25
Percent of Flights with Airborne Delay	56%	56%	83%
Average Energy on Airborne Delay (kWh)	2.96	4.47	5.07
Std. Dev. of Energy (kWh)	3.92	4.03	11.21

Results for the nominal demand scenario, with a demand rate of 10 aircraft per hour, per vertiport, are shown in Fig. 22 with corresponding data summarized in Table 11.

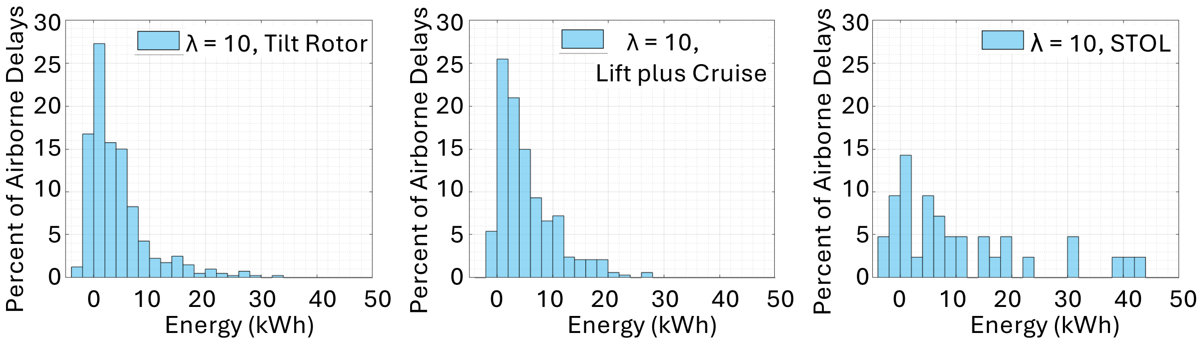

(a) Tilt Rotor eVTOL (b) Lift plus Cruise eVTOL (c) Blown-Flap eSTOL

Fig. 22 Energy spent on airborne delay per aircraft for demand scenario λ_v = 10, mixed fleet.

Similar trends to the low demand scenario are observed, though with a higher proportion of flights experiencing airborne delays. This is to be expected with an increase in demand on the system. The standard deviation of the energy caused by delay also rises for each aircraft type, indicating larger uncertainty in energy spent on delay with increased demand. Also, an increased percent of airborne delays result in a decrease in energy consumption for tilt-rotor vehicle, however this effect diminishes for the eSTOL vehicle.

Table 11 Summary of energy spent on airborne delay per aircraft for demand scenario λ_v = 10, mixed fleet.

Configuration	Tilt Rotor	Lift plus Cruise	eSTOL
Aircraft Count	512	435	44
Aircraft with Airborne Delay	400	334	42
Percent of Aircraft with Airborne Delay	78%	77%	95%
Average Energy on Airborne Delay (kWh)	4.19	5.40	10.47
Standard Deviation of Energy (kWh)	5.70	5.12	16.55

Figure 23 presents the results for the high demand scenario, with a λ_v of 15. In this scenario, over 90% of operations for each aircraft type are experience airborne delay.

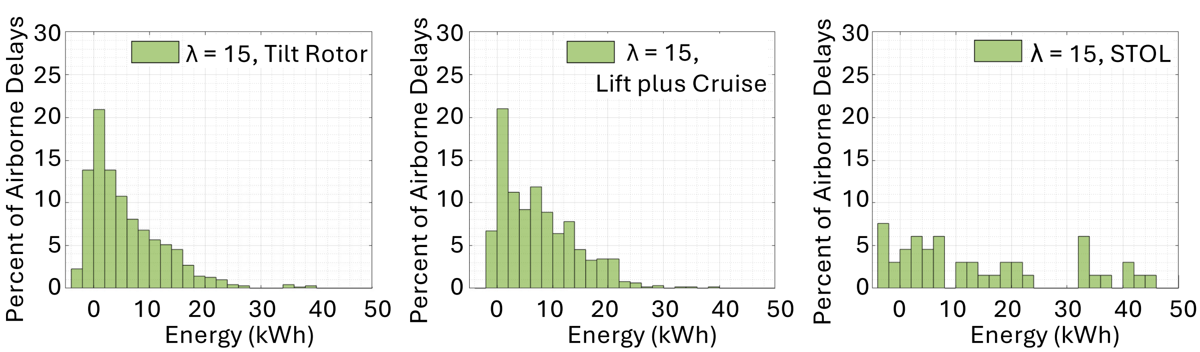

(a) Tilt Rotor eVTOL (b) Lift plus Cruise eVTOL (c) Blown-Flap eSTOL

Fig. 23 Energy spent on airborne delay per aircraft for demand scenario λ_v = 15, mixed fleet.

The results are summarized in Table 12 and suggest that the higher demand increases the average energy spent on delay across each vehicle type, aswell as increased standard deviation. These results reveal that increased demand levels lead to higher average energy consumption during airborne delays across all vehicle types. The associated standard deviations also increase, with the eSTOL vehicle exhibiting the highest variability.

Table 12 Summary of energy spent on airborne delay per aircraft for demand scenario λ_v = 15, Mixed fleet.

Configuration	Tilt Rotor	Lift plus Cruise	eSTOL
Aircraft Count	783	707	68
Aircraft with Airborne Delay	707	642	66
Percent of Aircraft with Airborne Delay	90%	91%	97%
Average Energy on Airborne Delay (kWh)	5.99	7.51	10.99
Standard Deviation of Energy (kWh)	7.30	6.75	27.40

Across each demand scenario, the tilt rotor and lift plus cruise configurations show similar percentages of flights encountering airborne delays, suggesting comparable system-level impacts of the speed-based conflict resolution algorithm. However, the eSTOL vehicle demonstrates a higher numbers of delays and greater energy variability, indicating less predictable performance, especially under congestion. This behavior is likely influenced by the eSTOL vehicle's higher cruise speed and more variable response to the speed-based tactical maneuvers, which can amplify both energy consumption and delay variability. These results highlight the importance of incorporating vehicle-specific performance into scheduling algorithms to minimize constraints imposed on faster vehicles by slower ones.

D. Vehicle Performance: Community Noise Impact

The community noise impact for the simulated scenarios is evaluated according to the $50N_{60}$ noise metric, which is defined as the observer area that exceeds 50 overflights recording atleast 60 dBA $L_{A,Max}$ within the simulated 12 hour duration. A map of the $50N_{60}$ noise contour area for the entire DFW AAM airspace construct is presented for the different demand scenarios in Figure 24 through Figure 27, presenting the comparison of a given demand scenario with the speed-based conflict resolution algorithm on and off. The total contour areas are summarized in Table 13.

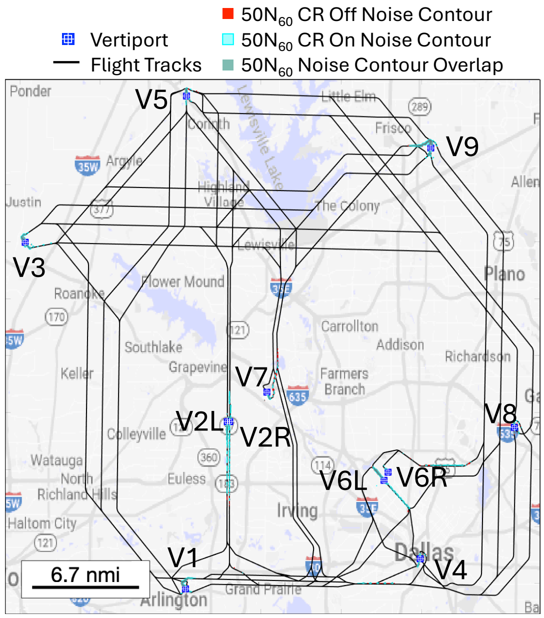

Fig. 24 50 N_{60} $L_{A,max}$ noise contour of full airspace for demand level λ_v = 6, mixed fleet.

The 50N_{60} contour areas are generally local to veriports, with some under track noise present on select routes. In the λ_v = 6 case in Fig. 24, there is undertrack noise presented for regions near V2L and V2R at DFW, and V6L and V6R at Dallas Love Field which are subject to class B altitude restrictions. Figure 25 presents the 50N_{60} noise contour area for the nominal demand rate with only one aircraft type. The resulting contours, when compared to the mixed fleet scenarios, present more variability.

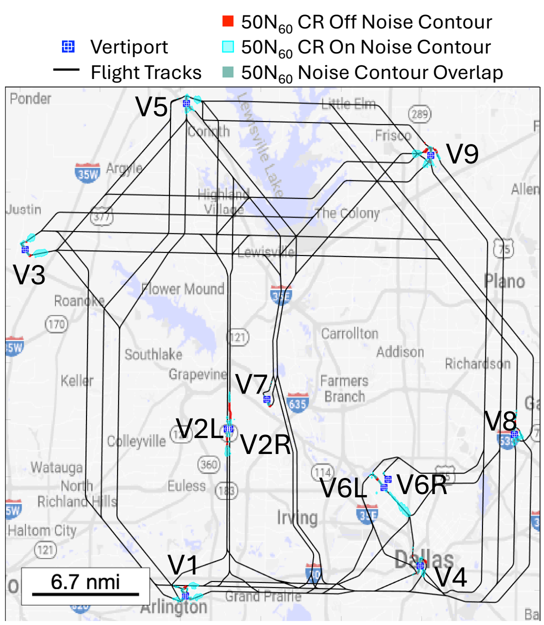

Fig. 25 50 N_{60} $L_{A,max}$ noise contour of full airspace for demand level λ_v = 10, one AC type.

The nominal demand rate of λ_v = 10 with a mixed aircraft fleet is presented in Fig. 26.

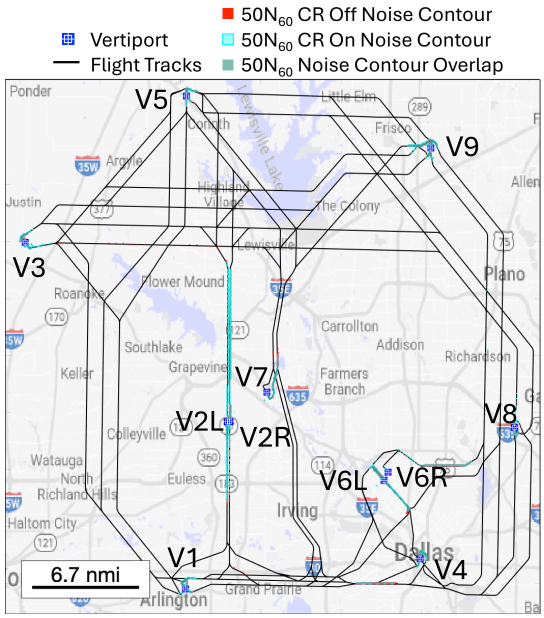

Fig. 26 50 N_{60} $L_{A,max}$ noise contour of full airspace for demand level λ_v = 10, mixed fleet.

With increased contours around vertiports, there is also more prominent undertrack noise contours present particularly for routes in the class B airspace (see Fig. 7), which have lower altitude restrictions of 900 - 1900 ft, depending on the location.

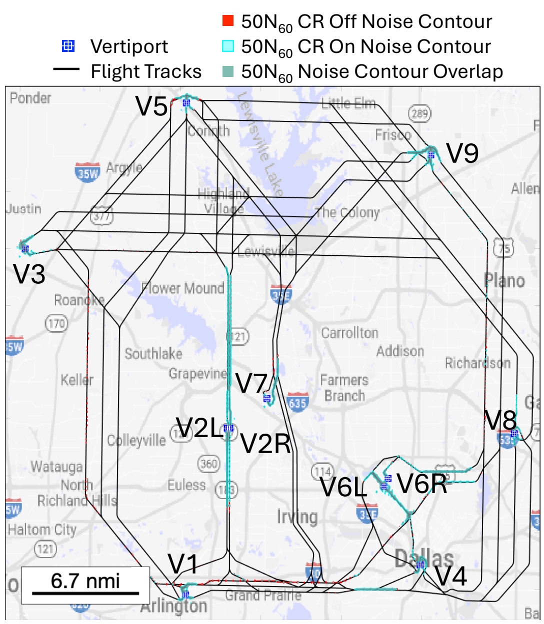

Fig. 27 50 N_{60} $L_{A,max}$ noise contour of full airspace for demand level λ_v = 15, mixed fleet.

Across the mixed fleet demand scenarios, employing the speed-based conflict resolution algorithm decreases the total contour area by 5 - 12 % depending on the demand rate whereas the scenario with one AC type exhibits a significant increase in contour area, as summarized in Table 13.

Table 13 Summary of total community noise contour areas for demand scenarios comparing community noise impact for CR on and CR off.

Demand Scenario	50 N_{60} Contour Area (nm^2) CR Off	50 N_{60} Contour Area (nm^2) CR On	50 N_{60} Contour Area (nm^2) Δ	50 N_{60} Contour Area % Difference
Mixed Fleet, λ_v = 6	0.0479	0.0421	-0.0058	-12.11%
Mixed Fleet, λ_v = 10	0.0808	0.0762	-0.0046	-5.69%
One AC Type, λ_v = 10	0.0161	0.0510	0.035	216.8%
Mixed Fleet, λ_v = 15	0.13	0.1099	-0.0201	-15.46%

The reduction in contour area observed for the CR On cases with mixed fleets is primarily attributable to decreasing thrust required to decelerate during a conflict resolution maneuver in cruise. Lower thrust levels lead to reduced under-track noise, as rotor noise decreases with reduced thrust demand. An exception occurs for the tilt-rotor aircraft when conflicts are resolved in lower speed regimes near the vertiport. To see this more clearly, Fig. 28 presents the $50N_{60}$ noise contour areas for each demand scenario in the vicinity of vertiport V9. This complex airspace presents multiple intersections. The inbound flights enter the vertiport from the north and depart to the south. There is an evident intersection of departing and arriving flights to the left of the vertiport, resulting in frequent conflict resolution maneuvers. For the mixed fleet scenarios (Fig. 28a-c), contour area near the vertiport exhibit minimal change between CR Off and CR On. The one AC type in Fig. 28d demonstrates a shift in affected regions, with an increased contour area when applying the speed-based conflict resolution strategy. This increase is attributed to the tilt-rotor aircraft entering the transition phase earlier along the trajectory when resolving a conflict. During transition, the rotor experiences crossflow, which, when combined with high thrust settings, leads to increased rotor noise.

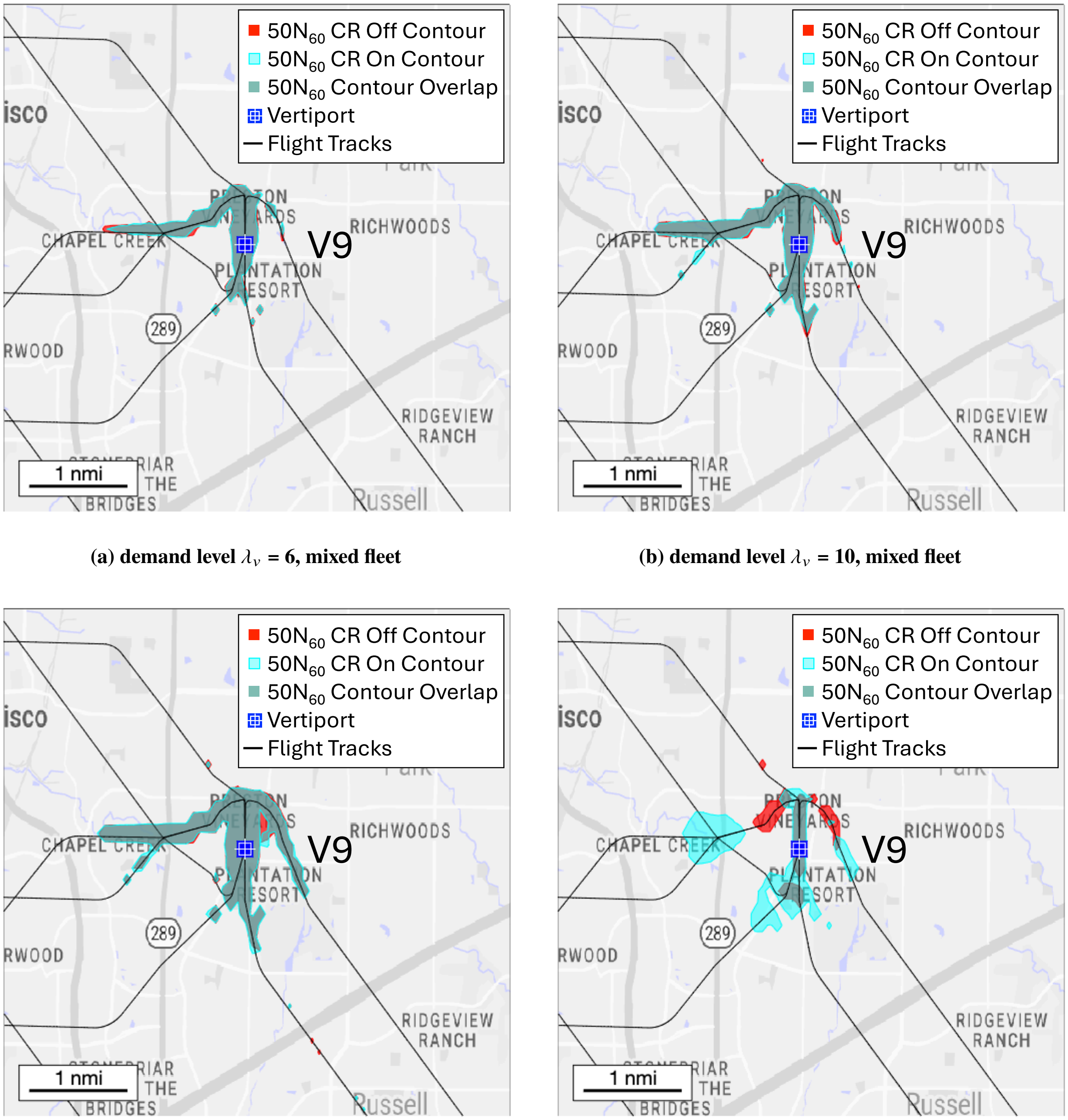

(a) demand level λ_v = 6, mixed fleet

(b) demand level λ_v = 10, mixed fleet

(c) demand level λ_v = 15, mixed fleet

(d) demand level λ_v = 10 one AC type

Fig. 28 50 N_{60} $L_{A,max}$ noise contours at vertiport V9 for different demand scenarios, comparing CR off and CR on.

VI. Conclusion

This work presents a methodology for evaluating vehicle performance within traffic flow management methods of an AAM airspace construct. By integrating detailed vehicle-specific performance models into the BlueSky air traffic simulator, this framework enables a detailed examination of operational trade-offs related to demand, scheduling, conflict resolution algorithms, energy consumption, and community noise exposure in a constrained urban airspace. The framework was applied to the Dallas/Fort Worth airspace across 12 scenarios with different traffic flow management initiatives, demand rates and fleet-mix. A demand scheduler and speed-based conflict resolution algorithm were developed and modeled, and the resulting ground and airborne delay, as well as additional energy consumption and community noise exposure was assessed. An AAM noise modeling methodology was demonstrated to determine community noise exposure for AAM operations, indicating primary noise exposure occurs at regions near vertiports, and applying a speed-based conflict resolution algorithm affects the noise exposure from aircraft types differently. Results revealed that the speed-based conflict resolution algorithm significantly affects both system-level and vehicle-level performance. While successfully resolving up to 93% of conflicts on arrival, the speed-based conflict resolution algorithm causes unresolved arrival conflicts to increase in severity. Additionally, conflicts caused by airspace constraints or between arrivals and departures were largely unmanaged, highlighting a limitation of the CR method. The conflict resolution increased energy consumption and variability across all demand levels and vehicle configurations, particularly for higher-speed aircraft such as the eSTOL configuration. These findings emphasize the necessity of integrating vehicle-specific performance considerations into TFM strategies to mitigate energy inefficiencies introduced by conflict resolution algorithms. Furthermore, they highlight the critical role of demand scheduling and trajectory planning in balancing safety, efficiency, and environmental impact in mixed-fleet AAM operations.

Overall, the demonstrated methodology for simulating AAM airspace integration with the effects of vehicle performance constraints provides a foundation for future research into performance-driven airspace design, enabling the safe and efficient integration of AAM vehicles into the national airspace system. The results from this analysis should not be generalized across different regions or TFM methods, but rather this framework can be adaptable to alternative advanced traffic flow management methods, scheduling algorithms, or new airspace constructs for other geographical regions to further study the adoption of AAM. Additionally, this modeling framework can be expanded to account for operational constraints at vertiports, including battery charging requirements or capacity limitations, as these factors critically influence overall system efficiency and throughput.

VII. Acknowledgments

This material is based upon work supported by the National Science Foundation Graduate Research Fellowship Program under Grant No. DGE-1839285. Any opinions, findings, and conclusions or recommendations expressed in this material are those of the authors and do not necessarily reflect the views of the National Science Foundation.

References

[1] United Nations, Department of Economic and Social Affairs, *World urbanization prospects: the 2018 revision (ST/ESA/SER.A/420)*, United Nations, New York, ISBN: 978-92-1-148319-2, 2019.

[2] Ahrenhold, N., Pohling, O., and Schier-Morgenthal, S., "Impact of Air Taxis on Air Traffic in the Vicinity of Airports," *Infrastructures*, Vol. 6, No. 10, October 2021, p. 140. https://doi.org/10.3390/infrastructures6100140.

[3] Raghunatha, A., Thollander, P., and Barthel, S., "Addressing the emergence of drones – A policy development framework for regional drone transportation systems," *Transportation Research Interdisciplinary Perspectives*, Vol. 18, March 2023, p. 100795. https://doi.org/10.1016/j.trip.2023.100795.

[4] Barbano, M., and Costa, V., "Implementing Urban Air Mobility in a Multi-Level Regulatory Framework: Perspectives from the EU," *2023 International Conference on Unmanned Aircraft Systems (ICUAS)*, Warsaw, Poland, June 2023, pp. 895–902. https://doi.org/10.1109/ICUAS57906.2023.10156184.

[5] Bauranov, A., and Rakas, J., "Designing airspace for urban air mobility: A review of concepts and approaches," *Progress in Aerospace Sciences*, Vol. 125, August 2021, p. 100726. https://doi.org/10.1016/j.paerosci.2021.100726.

[6] Garrow, L. A., German, B. J., and Leonard, C. E., "Urban air mobility: A comprehensive review and comparative analysis with autonomous and electric ground transportation for informing future research," *Transportation Research Part C: Emerging Technologies*, Vol. 132, November 2021, p. 103377. https://doi.org/10.1016/j.trc.2021.103377.

[7] Chin, C., Qin, V., Gopalakrishnan, K., and Balakrishnan, H., "Traffic management protocols for advanced air mobility," *Frontiers in Aerospace Engineering*, Vol. 2, May 2023, p. 1176969. https://doi.org/10.3389/fpace.2023.1176969.

[8] Vascik, P. D., and Hansman, R. J., "Scaling Constraints for Urban Air Mobility Operations: Air Traffic Control, Ground Infrastructure, and Noise," *AIAA Paper 2018-3849*, American Institute of Aeronautics and Astronautics, June 2018. https://doi.org/10.2514/6.2018-3849.

[9] Goyal, R., Reiche, C., Fernando, C., and Cohen, A., "Advanced Air Mobility: Demand Analysis and Market Potential of the Airport Shuttle and Air Taxi Markets," *Sustainability*, Vol. 13, No. 13, July 2021, p. 7421. https://doi.org/10.3390/su13137421.

[10] Mueller, E. R., Kopardekar, P. H., and Goodrich, K. H., "Enabling Airspace Integration for High-Density On-Demand Mobility Operations," *AIAA Paper 2017-3086*, Denver, Colorado, June 2017. https://doi.org/10.2514/6.2017-3086.

[11] Federal Aviation Administration, "Normalizing Unmanned Aircraft Systems Beyond Visual Line-of-Sight Operations," Final rule, *Federal Register*, Vol. 90, No. 150, pp. 38212–38391, August 2025. URL https://www.federalregister.gov/documents/2025/08/07/2025-14992/normalizing-unmanned-aircraft-systems-beyond-visual-line-of-sight-operations, accessed: 29 August 2025.

[12] Federal Aviation Administration, "Urban Air Mobility: Concept of Operations v2.0," Federal Aviation Administration, April 2023. URL https://www.faa.gov/sites/faa.gov/files/Urban%20Air%20Mobility%20%28UAM%29%20Concept%20of%20Operations%202.0_0.pdf, accessed: 29 August 2025.

[13] Vascik, P. D., and Hansman, R. J., "Constraint Identification in On-Demand Mobility for Aviation through an Exploratory Case Study of Los Angeles," *AIAA Paper 2017-3083*, June 2017. https://doi.org/10.2514/6.2017-3083.

[14] Federal Aviation Administration, "Engineering Brief No. 105A: Vertiport Design," Memorandum from Robert Bassey, P.E., AAS-110, Airport Engineering Division, December 2024, URL https://www.faa.gov/airports/engineering/engineering_briefs/eb_105a_vertiports, Accessed: 29 August 2025.

[15] Federal Aviation Administration, "Integration of Powered-Lift: Pilot Certification and Operations; Miscellaneous Amendments Related to Rotorcraft and Airplanes," Final rule, *Federal Register*, Vol. 89, No. 224, pp. 92296–92522, Nov. 2024. URL https://www.govinfo.gov/content/pkg/FR-2024-11-21/pdf/2024-24886.pdf, Accessed: 29 August 2025.

[16] Brown, A., and Harris, W., "A Vehicle Design and Optimization Model for On-Demand Aviation," *AIAA Paper 2018-0105*, Jan 2018. https://doi.org/10.2514/6.2018-0105.

[17] Tumuluru Ramesh, N., and V. Pandurangi, P., "A flight performance based optimization model for eVTOL vehicles," preprint, August 2022. https://doi.org/10.31224/2519.

[18] Ackerman, K. A., and Gregory, I. M., "Trajectory Generation for Noise-Constrained Autonomous Flight Operations," *AIAA Paper 2020-0978*, Jan 2020. https://doi.org/10.2514/6.2020-0978.

[19] Ackerman, K. A., Gregory, I. M., Theodorou, E., and Hovakimyan, N., "A Model Predictive Control Approach for In-Flight Acoustic Constraint Compliance," *AIAA Paper 2021-1958*, Jan 2021. https://doi.org/10.2514/6.2021-1958.

[20] Ackerman, K. A., and Gregory, I. M., "Comparison of Acoustic Models and Trajectory Generation Methods for an Acoustically-Aware Aircraft," *AIAA Paper 2023-2543*, Jan 2023. https://doi.org/10.2514/6.2023-2543.

[21] Johnson, W., "NDARC - NASA Design and Analysis of Rotorcraft," Tech. Rep. NASA/TP-2015-218751, Apr. April 2015.

[22] Lukaczyk, T. W., Wendorff, A. D., Colonno, M., Economon, T. D., Alonso, J. J., Orra, T. H., and Ilario, C., "SUAVE: An Open-Source Environment for Multi-Fidelity Conceptual Vehicle Design," *AIAA Paper 2015-3087*, June 2015. https://doi.org/10.2514/6.2015-3087.

[23] Hartman, D., Hartman, C. L., and Foster, J. V., "Performance Modeling of Urban Air Mobility Vehicles to Support Air Traffic Management Research," *AIAA Paper 2023-0548*, January 2023. https://doi.org/10.2514/6.2023-0548.

[24] Clarke, M. A., and Alonso, J., "Evaluating the Performance and Acoustic Footprint of Aircraft for Regional and Urban Air Mobility," *AIAA Paper 2021-3205*, August 2021. https://doi.org/10.2514/6.2021-3205.

[25] Vascik, P. D., and Hansman, R. J., "Assessing Integration Between Emerging and Conventional Operations in Urban Airspace," *AIAA Paper 2019-3125*, June 2019. https://doi.org/10.2514/6.2019-3125.

[26] Onat, E. B., Bulusu, V., Chakrabarty, A., Hansen, M., Sengupta, R., and Sridhar, B., "Evaluating eVTOL Network Performance and Fleet Dynamics through Simulation-Based Analysis," *AIAA Paper 2024-0336*, American Institute of Aeronautics and Astronautics, Orlando, FL, January 2024. https://doi.org/10.2514/6.2024-0336.

[27] Espejo-Díaz, J. A., Alfonso-Lizarazo, E., and Montoya-Torres, J. R., "A heuristic approach for scheduling advanced air mobility aircraft at vertiports," *Applied Mathematical Modelling*, Vol. 123, November 2023, pp. 871–890. https://doi.org/10.1016/j.apm.2023.07.009.

[28] Cheng, A. W., Witzberger, K. E., Isaacson, D. R., Verma, S. A., Arneson, H. M., Lee, H., Seah, C. H., Field, M., and Levitt, I., "National Campaign (NC)-1 Strategic Conflict Management Simulation (X4) Final Report," Tech. Rep. NASA/TM-2022-0018159, December 2022.

[29] Lee, H., Moolchandani, K. A., and Arneson, H., "Demand Capacity Balancing at Vertiports for Initial Strategic Conflict Management of Urban Air Mobility Operations," *2022 IEEE/AIAA 41st Digital Avionics Systems Conference (DASC)*, IEEE, Portsmouth, VA, USA, September 2022, pp. 1–10. https://doi.org/10.1109/DASC55683.2022.9925753.

[30] Hoekstra, J., and Ellerbroek, J., "BlueSky ATC Simulator Project: an Open Data and Open Source Approach," *7th International Conference on Research in Air Transportation: Philadelphia, USA*, 2016. URL https://pure.tudelft.nl/ws/files/10083831/Hoekstra_BlueSky_project.pdf.

[31] Jiang, X., Tang, Y., Cao, J., Bulusu, V., Yang, H. F., Peng, X., Zheng, Y., Zhao, J., and Sengupta, R., "Simulating Integration of Urban Air Mobility into Existing Transportation Systems: Survey," *Journal of Air Transportation*, Vol. 32, No. 3, Jul 2024, pp. 97–107. https://doi.org/10.2514/1.D0431.

[32] Sun, J., Ellerbroek, J., and Hoekstra, J., "OpenAP: An open-source aircraft performance model for air transportation studies and simulations," *Aerospace*, Vol. 7, No. 8, July 2020. https://doi.org/10.3390/aerospace7080104.

[33] Sun, J., Ellerbroek, J., and Hoekstra, J., "WRAP: An open-source kinematic aircraft performance model," *Transportation Research Part C: Emerging Technologies*, Vol. 98, Jan 2019, pp. 118–138. https://doi.org/10.1016/j.trc.2018.11.009.

[34] Pellerito, V. R., Yeung, N. H., Huynh, J. L., and Hansman, R. J., "Impact of Flight Trajectory Design on Performance and Noise for AAM Aircraft," *AIAA Paper 2024-4076*, July 2024. https://doi.org/10.2514/6.2024-4076.

[35] Yeung, N., la Cruz, J. D., Pellerito, V. R., Wang, Z., Lepe, M., Huynh, J. L., and Hansman, R. J., "Flight Procedure and Community Noise Modeling of Advanced Air Mobility Flight Vehicles," *AIAA Paper 2023-3361*, June 2023. https://doi.org/10.2514/6.2023-3361.

[36] De la Cruz, Jessica, "Methodology to Model Aircraft and Propulsor Performance of Advanced Air Mobility," Master's thesis, University of California, Irvine, Irvine, CA, June 2023, URL https://escholarship.org/uc/item/6tk8v3r6.

[37] Guerreiro, N. M., Hagen, G. E., Maddalon, J. M., and Butler, R. W., "Analysis of Strategic Conflict Management Approaches as Applied to Simulated UAM Operations," Tech. Rep. NASA/TM–20220017551, Hampton, VA, Apr. April 2023.

[38] Gonzalez, V. R., "A Methodology for Integrating Vehicle Performance into Traffic Flow Management Analysis for AAM Airspace Integration," Ph.d. thesis, University of California, Irvine, Irvine, CA, September 2025.

[39] De La Cruz, J. J., "Methodology to Model Aircraft and Propulsor Performance of Advanced Air Mobility," Master's thesis, University of California, Irvine, 2023. URL https://escholarship.org/uc/item/6tk8v3r6.

[40] John D. Anderson, J., *Aircraft Performance and Design*, McGraw-Hill, New York, 1999.

[41] Bacchini, A., and Cestino, E., "Electric VTOL Configurations Comparison," *Aerospace*, Vol. 6, No. 3, February 2019. https://doi.org/10.3390/aerospace6030026.

[42] "Joby Aviation," , Joby Aviation, 2025. URL https://www.jobyaviation.com, accessed: 11 June 2025.

[43] Courtin, C., Mahseredjian, A., Dewald, A. J., Drela, M., and Hansman, J., "A Performance Comparison of eSTOL and eVTOL Aircraft," *AIAA Paper 2021-3220*, June 2021. https://doi.org/10.2514/6.2021-3220.

[44] Courtin, C. B., "Performance, Stability and Control of Electric Short Takeoff and Landing Aircraft," Ph.d. thesis, Massachusetts Institute of Technology, Cambridge, MA, May 2024. URL https://hdl.handle.net/1721.1/155476.

[45] Vertical Flight Society, "Joby S4," , 2023. URL https://evtol.news/joby-s4, accessed: 27 August 2025.

[46] International Civil Aviation Organization (ICAO), "Global Air Traffic Management Operational Concept," Tech. Rep. ICAO, Doc. 9854, First Edition, 2005. URL https://www2023.icao.int/Meetings/anconf12/Document%20Archive/9854_cons_en%5b1%5d.pdf.

[47] Badea, A. C. A., "Conflict Detection and Resolution for Constrained Urban Airspace," Ph.D. thesis, Delft University of Technology, Delft, The Netherlands, February 2025. https://doi.org/10.4233/uuid:5d40d6b6-7ac3-49c3-9fa4-e8858b6db451.

[48] Drela, M., and Youngren, H., "XROTOR User Guide," Massachusetts Institute of Technology, Cambridge, MA, 2003, URL https://web.mit.edu/drela/Public/web/xrotor/xrotor_doc.txt.

[49] Lopes, L. V., and Burley, C. L., "ANOPP2 User's Manual: Version 1.2," NASA TM 2016-219342, 2016.

[50] Krishnamurthy, S., Tuttle, B. C., and Rizzi, S., "A Synthesis Plug-in for Steady and Unsteady Loading and Thickness Noise Auralization," AIAA Aviation 2020 Forum, 2020. https://doi.org/10.2514/6.2020-2597.

[51] NASA Earthdata, "Earthdata," https://www.earthdata.nasa.gov, 2025. Accessed: 2025-06-12.

[52] Yu, A. Y., and Hansman, R. J., "Approach for Representing the Aircraft Noise Impacts of Concentrated Flight Tracks," *AIAA Paper 2019-3186*, June 2019. https://doi.org/10.2514/6.2019-3186.